Effect of *In Situ* Thermal Annealing Process on Structural, Optical and Electrical Properties of CdS\CdTe Thin-Film Solar Cells Fabricated by Pulsed Laser Deposition

By

Alaa Ayad Khedhair Al-Mebir

Submitted to the graduate degree program in Physics Science and the Graduate Faculty of the University of Kansas in partial fulfillment of the requirements for the degree of Master of Philosophy.

_____

Chairperson:

Distinguished Professor: Wu, Judy Z.

_____

Professor: Murray, Michael J.

_____

Assistant Professor: Chan, Wai-Lun

_____

Assistant Professor: Guanggen Zeng

Date Defended: June 10, 2015

The Thesis Committee for Alaa Ayad Khedhair Al-Mebir

certifies that this is the approved version of the following thesis:

Effect of *In Situ* Thermal Annealing Process on Structural, Optical and Electrical Properties of CdS\CdTe Thin-Film Solar Cells Fabricated by Pulsed Laser Deposition

Chairperson:

Distinguished Professor: Wu, Judy Z.

Date approved: June 10, 2015

ABSTRACT

Cadmium Telluride has long been recognized as the second lowest- cost material after Si in the world photovoltaic market, specifically for thin-film solar cells. The two attractive properties of the CdTe are its nearly ideal band gap of ~1.5 eV for single p-n junction photovoltaic and its high optical absorption coefficient up to 10^5 cm^{-1}. Therefore, a thickness of ~1 μm of CdTe can absorb up to 90% of the incident light.

The key to high-performance thin film CdTe-based solar cells is controlling microstructure of the CdS/CdTe through obtaining high-quality crystalline CdTe thin films that have low density pinholes and other defects and form high-quality p-n heterojunction interfaces on the CdS or other window layers. Considering these, the relative high temperatures used for CdTe thick film growth may not be suitable in the thin film case due to lack of control in CdTe microstructure evolution. Therefore, development of low-temperature processes for CdTe thin film solar cells is important to achieving a precise control of the CdS/CdTe microstructure and optoelectronic properties. In addition, low temperatures provide benefits in wider selection of substrates especially those for low-cost, flexible solar cells applications. However, the CdS/CdTe solar cells based on thin CdTe films fabricated at low temperature have generally poor performance as a result of increased density of grain boundaries and defects. In order to address this issue, we have developed an *in situ* thermal annealing process (iTAP) immediately after the CdS/CdTe deposition using Pulsed laser deposition (PLD) at 200 °C and before the common *ex situ* $CdCl_2$ annealing typically employed for optimization of the CdTe-based solar cells. A systematic study on the microstructure, optical and optoelectronic properties of CdS/CdTe solar cells processed under different iTAP conditions has been carried out. It has been found that these physical properties depend sensitively on the iTAP processing conditions

and appropriate iTAP in the optimal window enhances grain growth, improves grain boundary connectivity, and reduces crystal defects. This leads to considerably improved CdTe crystallinity and as a result, improved optoelectronic properties of the CdS/CdTe solar cells. Our result suggests that the iTAP is important for optimizing the chemical composition and microstructure of CdTe thin films and its heterojunction with CdS, both of which are critical to the performance of the CdS/CdTe thin film solar cells. In addition, it was found that smaller CdTe thickness provides advantages in reduced charge recombination.

ACKNOWLEDGEMENTS

I have hesitated in writing these acknowledgements, for the difficulty in adequately expressing what should be said and inevitability of forgetting someone or some contributions. Therefore, I must apologize in advance for anyone I have missed.

First of all, I would like to be thankful to Allah, to whom all things return, for lighting my education journey and increasing my knowledge and for everything I have achieved so far.

Also, I wish to extend my deep appreciation to my advisor Prof. Judy Wu. She has had a tremendous effect on the success of my research and has provided me with all the knowledge I needed to complete my thesis and publications. I'm grateful for her constructive guidance and advices throughout every step in my research. Without her advices and contribution, this work would not be in this status. Next, I would like to sincerely thank my sponsor, the Higher Committee for Education Development in Iraq (HCED), represented by Dr. Zuhair Humadi and all the staff members for their supports.

I would like to thank my fellow students and friends; Wade Rush and his wife Sara for their time and advices; Paul Harrison, Ali Saber, and Dr. Zeng for providing me with valuable information during my research; the faculty and staff members in the department of Physics and Astronomy at the University of Kansas for making the journey in my master program such a great experience.

Lastly, and most importantly, I would like to thank my father for opining my eyes to education and science, for getting me involved with a wide array of actual hands on learning from an early age; my mother for her constant warmth and prayers; my brothers; my sisters and my relatives. I'm thankful for all their support. What a blessing it is to have them in my life.

Alaa Ayad Al-Mebir /June 10, 2015

TABLE OF CONTENTS

LIST OF FIGURES

LIST OF TABLES

Chapter 1 : Solar Cells Developments

1.1: Introduction

1.1.1: Energy Definition

The most abstract definition of energy is that it is a certain quantity that does not change in the manifold changes which nature undergoes. It is stated that since it is a mathematical principle, there is a numerical quantity which invariant when something happens. This fact is also called the conservation of energy. We cannot describe it as a mechanism, or anything concrete, it is just a fact that we can calculate the same number before and after any changes in nature. Although in physics we have no knowledge of what energy is, we can use some formulas to calculate some numerical quantities, and when we add them all together, we can see that they are conserved. Energy has a large number of different forms with different formulas, such as gravitational energy, kinetic energy, heat energy, elastic energy, electrical energy, chemical energy, radiant energy, nuclear energy and mass energy [1].

The unit of Joule (J), named according to the English physicist James Prescott Joule (1818-1889), is often used to measure energy. This unit is defined as the amount of energy required to apply (1 Newton) of force on (1 meter of distance), that means:

$$1\ J = 1\ N.m \tag{1.1}$$

Energy is also related to another important physical quantity which is power (P). The power p is defined as the rate of doing work, or the amount of energy consumed per unit time, therefore:

$$E=\int P(t)dt \tag{1.2}$$

The power is usually measured in Watt (W) unit, according to the Scottish engineer James Watt (1736-1819), where (1 W) is one Joule per second, (1 W = 1 J/s) or (1 J = 1 W.s). In some energy forms, such as the electricity, often the unit Kilowatt hour (kWh) is used. It is given as:

$$1\text{kWh} = 1000\text{Wh} \times 3600\,\frac{\text{s}}{\text{h}} = 3.600.000\ \text{W.s} \tag{1.3}$$

Also, there is another unit to measure small amount of energy in solid state physics, which is the unit of electron volt (eV). This unit is defined as the amount of energy gained or lost by the charge of a single electron ($e = 1.602 \times 10^{-19}\text{C}$) moved across an electric potential difference of one volt (V), therefore:

$$1\ \text{eV} = 1.602 \times 10^{-19}\ \text{J} \tag{1.4}$$

1.1.2: Energy Consumption

The different forms of energy mentioned before are consumed for many different purposes. For example, we use energy for heating buildings, houses and water. For transportation, we use a lot of energy to run cars, trains, trucks and planes. We use energy to produce most of our daily life stuff and also to produce food. Energy involves in almost everything in our life, especially in the most prosperous and technologically developed nations like the USA, where energy is consumed widely. World Energy Statistics of 2013 shows that the average U.S. citizen uses an average power of (9319 W). While, an average citizen from India only uses about (800 W) [2], which is less than a tenth of the U.S. consumption. Figure 1-1: shows the world total final consumption from 1971 to 2012 by fuel in "million tonnes of oil equivalent (mtoe) unit". This statistic stated that the world consumption energy doubled over the last 40 years.

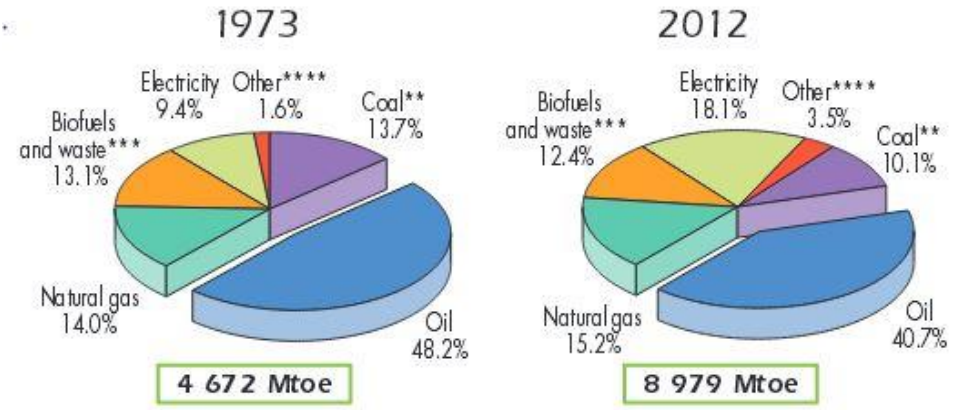

Figure 1-1: World total fuel energy consumption from 1973 to 2012 [3].

Besides increasing living standards in the modern and developed societies, the increment of energy consumption is due to the rapidly growth of world population. Studies predict a world population of 9 billion around 2040 in contrast to the 7 billion people in 2013. Therefore, the global energy demand is increasing.

Moreover, another challenge related to energy consumption is that the dependence on fossil fuels energy source such as oil, coal and gas, which are not renewable and have huge impacts on the climate change. Burning fossil fuels produces the so-called greenhouse gases like carbon dioxide (CO_2). The additional carbon dioxide created by using these energy sources is stored in our oceans and atmosphere, which is responsible for the global warming and climate change [4]. In Figure 1-2, we can notice the increase in carbon dioxide concentration in (million tonnes unit (Mt)) in the Earth's atmosphere from 1971 to 2012.

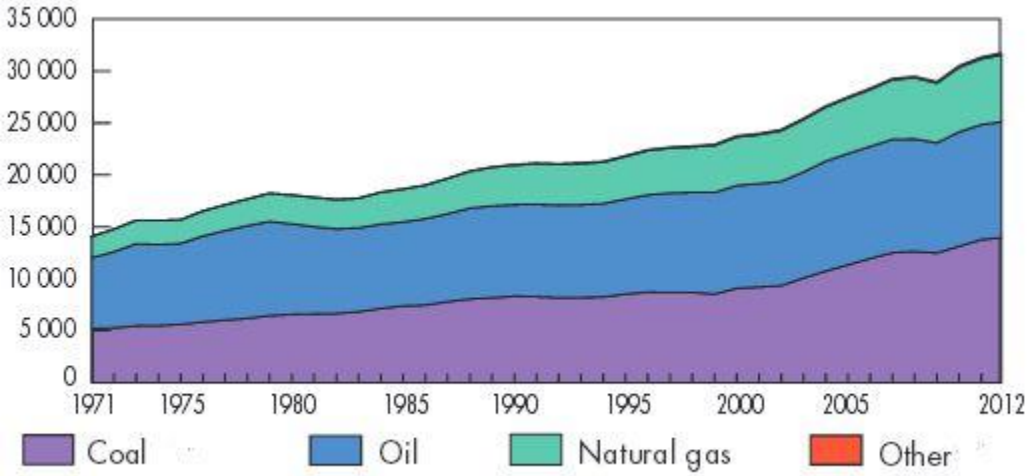

Figure 1-2: World CO_2 emissions from 1971 to 2012 by fuel (Mt of CO_2) [3].

1.1.3: Sources and Forms of Energy

The different energy forms which were mentioned in the previous section can be converted from one form to another, and they are produced by different sources. As it is showed in Figure 1-3, there are three major sources of energy [5]. First energy source is the chemical energy stored in fossil fuels. This energy is converted to thermal energy by burning, with efficiency up to 90%. Then, the thermal energy can be converted into mechanical energy by using heat engines which have conversion efficiency up to 60%. This principle is used in our daily life in most of transportations such as to operate cars and planes. Finally, mechanical energy can be converted into electrical energy by using electrical generators with efficiency about 90%. A turbo generator that is connected to a steam turbine is usually used in most of electricity stations around the world, where the major energy source is coal. From what is stated in these conversion steps, it is well known that when the fossil fuels are used to generate electricity, more than 50% of the chemical efficiency is lost into the environment in form of heat.

Also, producing the energy from this source has huge impacts on the climate change because of the carbon emissions which result during these processes. The second energy source is nuclear energy in which energy is released as thermal energy during nuclear fission reactions. This thermal energy generates heat steam to operate a steam turbine which led to generate electricity. In this way, the carbon emissions which result from fossil fuel sources have been reduced. Although using the nuclear sources to generate electricity is considered a good method to reduce carbon emissions, the political considerations have limited it, considering its massive accidences which have been occurred.

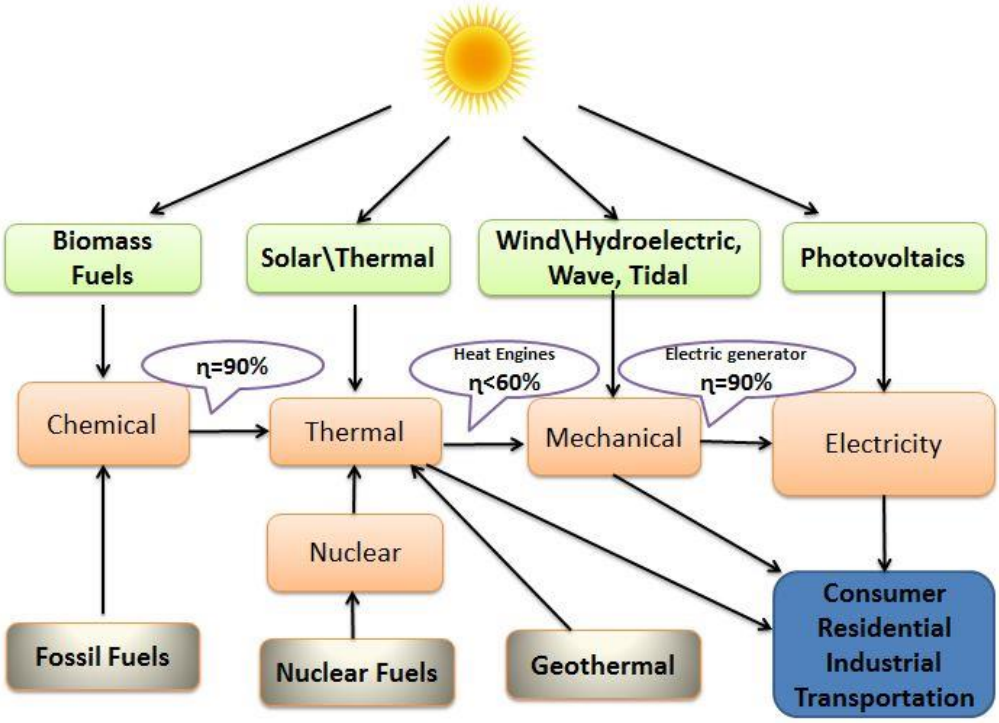

Figure 1-3: The Energy forms and the conversion methods between them.

So far the energy sources discussed above are not sustainable or renewable energy. This means that the fuel and nuclear sources are not produced by nature as much as their

consumption, which means that they will run out someday. The renewable energy is the third type of energy sources, in which the sun is the main source. This energy source can be converted to electricity directly without any gas emissions. More details about the renewable energy and how it is related to the electricity will be discussed in the next section.

1.1.4: Renewable Energy Options

The renewable energy source has been identified as the promising source to generate energy. It can be seen in Figure 1-3 that the sun energy is converted to many different forms of energy. For example, the sun energy can be converted directly to thermal energy and electricity, or indirectly in the form of wind, hydro and biomass fuels. Moreover, there are two other energy sources that are often considered as renewable in terms of their sustainable nature. The first one is energy in the tides caused by the gravitational fields of the moon and the sun which can be tapped using tidal barrages or tidal stream technology. The second source is geothermal energy from the earth's core accessible in some locations through hot springs, geezers or boreholes. However, the available average power produces from these energy sources is small comparable of that available from the sun.

From what is discussed so far, it is clear that the sun energy is the best sustainable energy source that can be converted to many different energy forms. One of these forms is electricity which is the second consumed energy in the world as it was shown in Figure 1. It has been used since at least 100 years now. It provides us with many energy forms that we need to use every day, and the access to it strongly determines the living standard.

Further, if the sun energy is converted into electricity directly using devices based on semiconductor materials, we call it photovoltaic (PV). The name photovoltaic comes from the Greek word (*phos*), which means light, and (*volt*), which refers to electricity. The word (*volt*) is named after the Italian physicist Alessandro Volta (1745-1827) who invented the battery. In the commercial solar modules, typical photovoltaic cells efficiencies are in the range of 15-20%.

1.2: Basics of Solar Cells

1.2.1: Historical Introduction

In 1839, the photovoltaic (PV) effect was first discovered by the French physicist Alexandre-Edmond Becquerel at an age of 19 years [6, 7]. He observed this effect while he was experimenting with an electrolytic cell. The electrolytic cell was made up of two platinum electrodes placed in an electrolyte which is an electrically conducting solution. Becquerel observed that when the cell exposed to light, the current of the cell was increased. In 1876, the British natural philosopher William Grylls Adams and his student Richard Evans Day discovered that selenium produces the photovoltaic effect when exposed to light, but with a very poor performance. Seven years later, the American inventor Charles formed photovoltaic junctions by coating selenium with an extremely thin layer of gold, and the energy conversion efficiency was 1% [8]. In 1905, Albert Einstein published his paper in which he explained the photoelectric effect on a quantum basis [9]. He assumed that light energy is being carried with quantized packages of energy, which called photons. The first silicon solar cell was invented by Russell Ohl in 1941[10]. Furthermore, the real development of modern solar cell technology began in 1954, when Daryl M. Chapin, Calvin S. Fuller, and Gerald L. Pearson demonstrated a silicon-

based solar cell with an efficiency of about 6% [11]. In the same year, the photovoltaic effect of II-VI semiconductor materials such as cadmium sulfide (CdS) has been reported by Reynolds et al. [12]. In 1956, the first gallium arsenide (GaAs) solar cell was reported with a photo-conversion efficiency of 6.5% [13]. The first polycrystalline thin film solar cells based on a cadmium-sulfide (CdS) / copper sulfide (Cu2S) junction with conversion efficiency up to 9.15% and areas of ~1 cm^2 was reported at the University of Delaware in 1980 [14]. In 1985, A. W. Blakers and M. A. Green reported crystalline silicon solar cells with efficiencies above 20% at the University of New South Wales in Australia [15]. After that, the multi-junction solar cells were introduced with high conversion efficiency. They can be described as a series of p-n junction photodiodes which have different band gaps. They have made of different III-V or II-VI materials such as gallium arsenide (GaAs), gallium indium phosphide (GaInP), copper indium diselenide (CIS), copper indium gallium diselenide (CIGS), and cadmium telluride (CdTe). First two-junction tandem photovoltaic device which was made of a lower GaAs layer and an upper GaInP layer has been reported by Jerry Olson in 1987 [16, 17], with photo-conversion efficiency up to 29.5% under concentrated solar light. Adding third additional junction for a GaInP/GaAs/Ge solar cell further increased the conversion efficiency up to 34% [18], and to 40% for a GaInP/GaAs/GaInAs cell [19]. It is also believed, according to theoretical calculation, that the conversion efficiency of multi- (or more) junction solar cells can be increased up to 55% [20]. However, the solar cell global market has been dominated by silicon flat panel modules, except for space applications, since their price is much lower than the use of arsenides and phosphides as photovoltaic (PV) devices.

In addition, environmental and economic issues have been very serious problems in all over the world since 2000, which led to increase the investment of solar energy. Therefore, the installed PV capacity has grown significantly between 1999 and 2013 as it shown in Figure 1-4. It can be shown in this figure that the world's cumulative installed PV capacity was more than 23 GW at the end of 2009. One year later, in 2010, it became 40.3 GW and the growth reached 70.5 GW in 2011. In 2012, 100GW was reached and by 2013, around 138.9 GW of PV had been installed around the world.

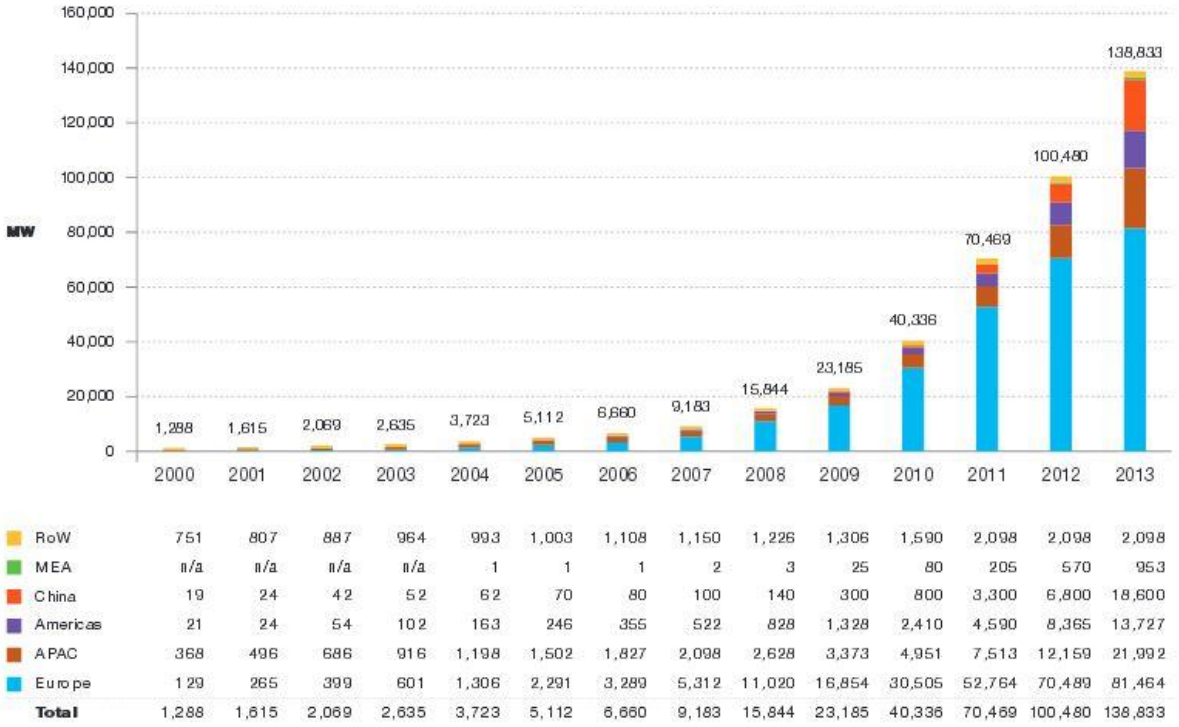

	2000	2001	2002	2003	2004	2005	2006	2007	2008	2009	2010	2011	2012	2013
RoW	751	807	887	964	993	1,003	1,108	1,150	1,226	1,306	1,590	2,098	2,098	2,098
MEA	n/a	n/a	n/a	n/a	1	1	1	2	3	25	80	205	570	953
China	19	24	42	52	62	70	80	100	140	300	800	3,300	6,800	18,600
Americas	21	24	54	102	163	246	355	522	828	1,328	2,410	4,590	8,365	13,727
APAC	368	496	686	916	1,198	1,502	1,827	2,098	2,628	3,373	4,951	7,513	12,159	21,992
Europe	129	265	399	601	1,306	2,291	3,289	5,312	11,020	16,854	30,505	52,764	70,489	81,464
Total	1,288	1,615	2,069	2,635	3,723	5,112	6,660	9,183	15,844	23,185	40,336	70,469	100,480	138,833

Figure 1-4: Global PV cumulative installed capacity from 2000 to 2013 [21].

1.2.2: Solar Spectra

Surface temperature of the sun is approximately 5800 K and its radiation spectrum can be approximated by a black body radiator at that temperature (as shown in Figure 1-5). Emission of radiation from the sun is isotropic like all black body radiators [22]. However, the great distance between the earth and the sun, which is approximately 93 million miles or 150 million kilometers, means that only those photons emitted directly at the Earth will contribute to the solar spectrum. On the other hand, the solar radiation is attenuated when passing through the atmosphere of the Earth. So, the most important factor that determines the solar irradiance under good sky conditions is the distance that the sunlight has to travel through the atmosphere. This distance is optimal when the Sun is directly overhead i.e.at the zenith. The ratio of an actual path length of the sunlight to this minimal distance is known as the optical air mass (AM). This air mass is a measure of the attenuations in spectral content and intensity of the solar radiation due to the atmosphere before reaching the Earth's surface. If the Sun is at its zenith the optical air mass is unity and the spectrum is called the air mass 1 (AM1) spectrum. And if the Sun is at an angle (θ) with the normal, the air mass is given by:

$$\text{Air mass} = 1/\cos\theta \tag{1-5}$$

A globally used standard for comparing solar cell performance is the AM1.5 ($\theta = 48.2^{\circ}$) spectrum normalized to a total power density of 1 kW/m^2.

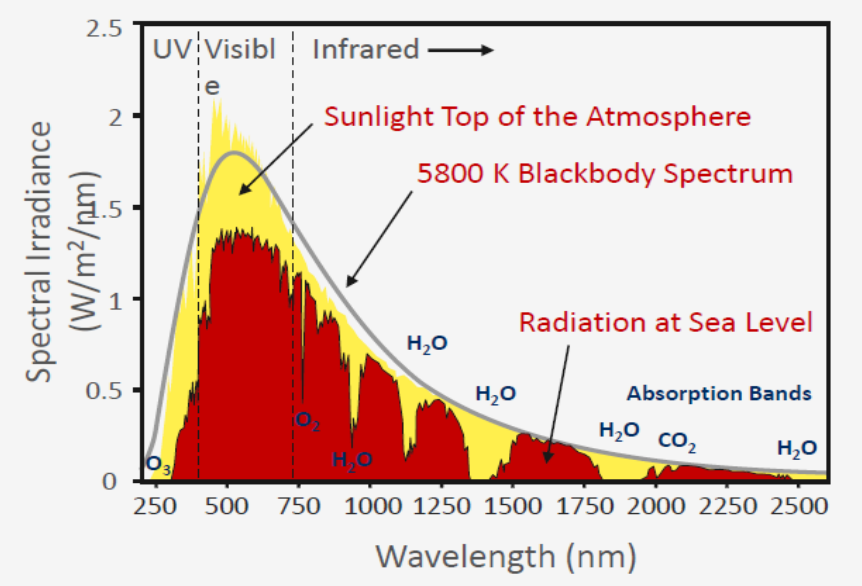

Figure 1-5: Solar spectra at different conditions [23].

In addition, the attenuation of solar radiation can be due to scattering, reflection and absorption by air molecules, dust particles and surrounding landscape, such as steam (H_2O), oxygen (O_2) and carbon dioxide (CO_2). Ozone absorbs radiation with wavelengths below 300 nm (UV). CO_2 molecules contribute to the absorption of solar radiation at wavelengths above 1 µm (infrared). All these attenuations can account for up to 49% of the light incident on a solar cell.

1.2.3: Working Principle of Solar Cells

The working principle of solar cells is based on the photovoltaic effect, in which a potential difference is generated at the junction of two different semiconductor materials that has absorbed light. In 1905, Albert Einstein explained this effect by assuming that the light consists of well-defined energy quanta, which so-called photons. The energy of one photon is given by:

$$E = h\nu \tag{1.6}$$

Where h is Planck's constant and ν is the frequency of the light.

There are three basic processes for the photovoltaic effect to be done. First process is generation of charge carriers when a photon, light, is absorbed in the materials, and second is separation of the photo-generated charge carriers in the junction between these materials, and finally is collection of the photo-generated charge carriers at the terminals of the junction.

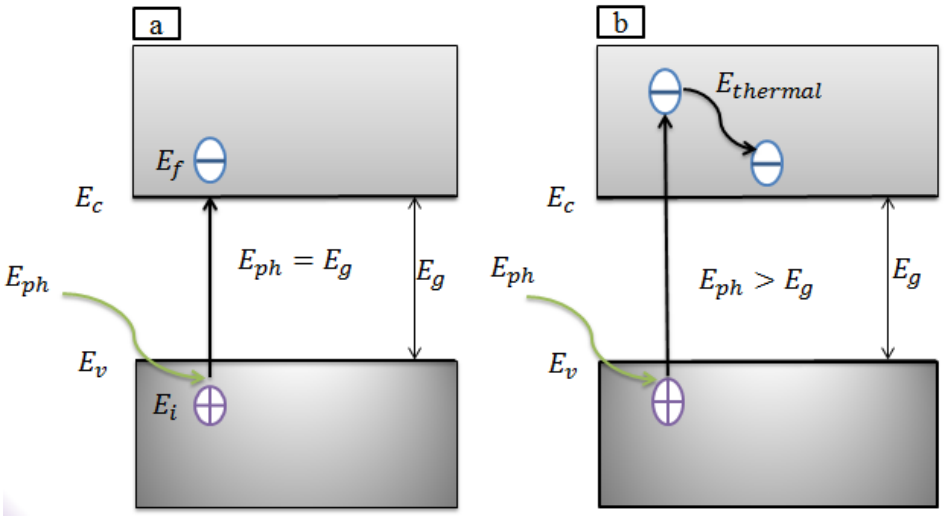

Figure 1-6: Photons' absorption in semiconductor materials have E_g band gap when a) $E_{ph} = E_g$, and b) $E_{ph} > E_g$.

As it is shown in Figure 1-6a, generation of charge carrier is resulted from absorption of a photon in semiconductor materials. It means that the photon energy is used to excite an electron from an initial state (E_i) to a final state (E_f). If the incident photon has energy higher than the difference between these two states, electron will be exited to higher level and eventually will move to the relaxation state by emitting thermal energy as shown in Figure 1-6b. In solid state physics, this can be understood based on band theory of solids states in which electrons of atoms in solids occupy states in energy bands.

The occupied band with the highest energy (E_v) is the valence band in which valence electrons, which are involved in the covalent bonds, have their allowed energies. The conduction

band, unoccupied band, is located above the valence band with energy (E_c). It is formed by the allowed energies of electrons liberated from the valance band. The energy difference between the edges of these two bands is known as the band gap energy (E_g). In a perfect solid, the energy states between the valence band and the conduction band are forbidden and not occupied. The energy band structure is considered an important parameter in studying material properties of solids. Figure 1-7: illustrate the difference between the band structure of conductors, insulators, and semiconductors materials.

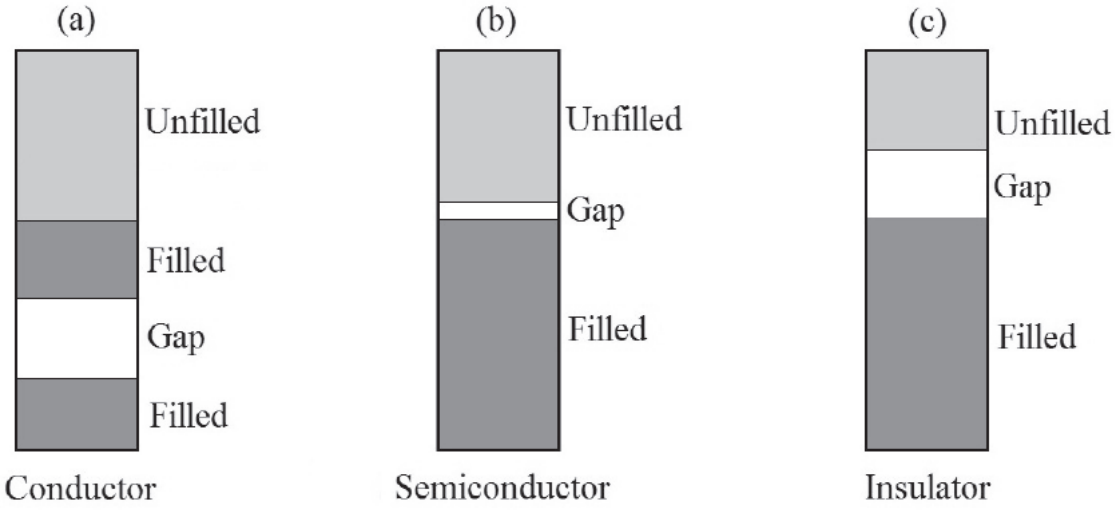

Figure 1-7: Simplified band structures of solid [24].

For conductors, the highest occupied energy level is in the middle of an energy band. In a pure semiconductor at absolute zero, no electrons are present in the conduction band and it behaves like an insulator. However, increasing temperature allows for thermal energy to excite electrons into the conduction band forming holes behind in the valence band. Excited electrons and resulting holes are so-called charge carriers and are considered as the main contributors to electric current.

The electrons transition from the valence band to the conduction band can be either direct or indirect, which is depending on the position of both the conduction and valance bands on semiconductor material. The band structure of a direct and indirect band gap semiconductor is shown in Figure 1-8. Usually direct band gap semiconductors are desirable for photovoltaic applications such as solar cells, because it is easy to excite electrons directly to the conduction band without the need of momentum energy. Therefore, the absorption coefficient of semiconductor material which strongly affects the performance of the devices is determined by its electronic structure. For example, semiconductor materials with direct band gaps such as GaAs and CdTe usually have high absorption coefficients, while those with indirect band gaps, like Si, suffer from low absorption coefficients.

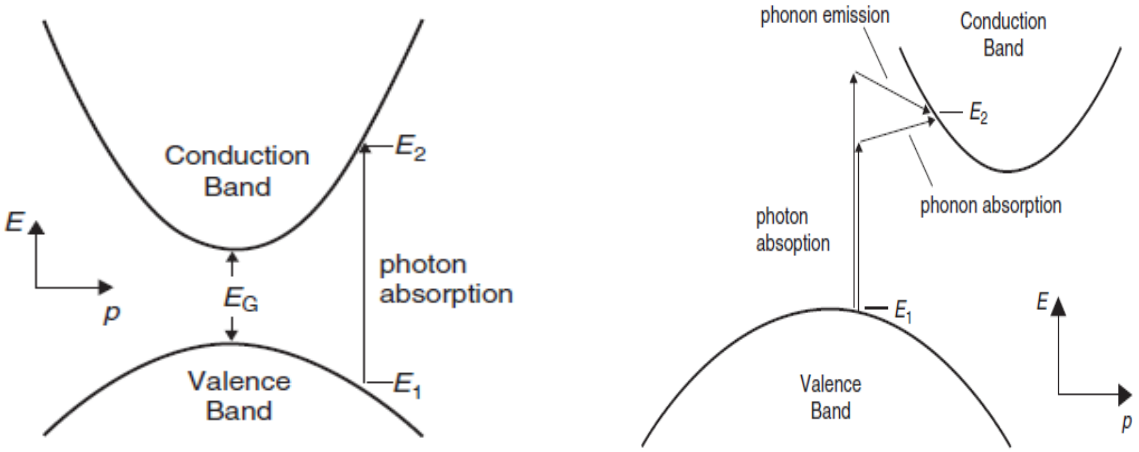

a) Direct band gap structure b) Indirect band gap structure

Figure 1-8: An energy band diagram for a) a direct band gap semiconductor and b) An indirect band gap semiconductor [22].

Semiconductor doping using impurity atoms is usually used to achieve specific semiconductor properties. These impurity atoms can donate or accept electrons in the valence

band. When doped semiconductors have penalty of holes, they are called p-type semiconductors. While, doped semiconductors that have penalty electrons are called n-type semiconductors. By placing two p-type and n-type semiconductors together, a p-n junction is formed. If the same material is used for the p-type and n-type of the junction, it is called a homojunction. However, if dissimilar semiconductors are used, it is called a heterojunction.

1.2.4: The P-N Junction Formation

The p-n junction is an important concept that allows solar cells to generate electric current. When a p-type semiconductor and an n-type semiconductor are brought together, there is a very large difference in electron concentration between these regions which causes a diffusion current of electrons from the n-type material across the p-n junction into the p-type material. Similarly, the difference in holes concentration causes diffusion current of holes from the p-type to the n-type material. Because of this diffusion process, the region close to the p-n junction becomes almost completely depleted of mobile charge carriers. The gradual depletion of the charge carriers produces a space charge created by the charge of the ionized donor and acceptor atoms that is not occupied by the mobile charges any more. This region of the space charge is so-called the *space-charge region* or *depleted region* and is schematically illustrated in Figure 1-9a.

The space charge around the p-n junction produces an internal electric field which forces the charge carriers to move in the opposite direction of the concentration gradient. The diffusion currents continue to flow until the concentration diffusion and the internal electrical field, drift, equal to each other. This case describes the equilibrium in which no net current flows through the p-n junction.

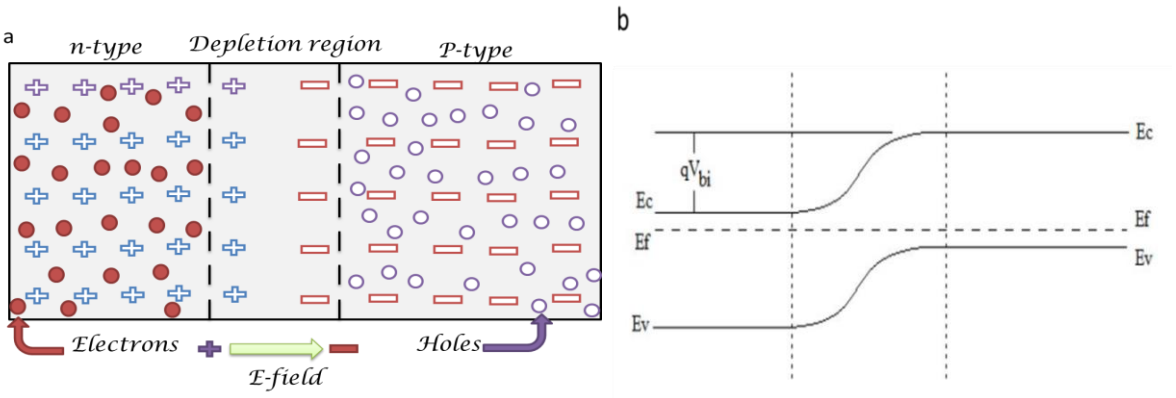

Figure 1-9: Diagram of a p-n junction.

Also, in a *p*-type semiconductor, the Fermi level, which is the energy level that has a 50% probability of getting occupied by an electron at any temperature, is close to the top of the valence band while the Fermi-level of an *n*-type semiconductor is close to the bottom of the conduction band. Therefore, when the p-n junction is formed between n- and p-type regions, there is a difference between the Fermi levels of the two sides which led the Fermi levels to be aligned as it is shown in figure 1-9b [24].

In solar cells design, sunlight is incident on the n-type layer which is called the window layer. This layer has a relatively high band gap compared to photons energy of sunlight. Ideally, all photons should pass through the n-type layer and are then absorbed in the p-type layer which has a band gap similar to the incident photons. The absorbed photons in the absorption layer generate free charge carriers, electrons-hole pairs, which are responsible to produce an electric current. The electric field in the depletion region drives electrons to the n-type layer and holes to the p-type layer. These charge carriers are then collected in the terminals of the front and back contacts of the device resulting in an electric current.

1.2.5: The Shockley-Queisser Limit

The theoretical limit for single-junction solar cells is usually referred to as the Shockley-Queisser (SQ) limit. In principle and as it discussed in Figure 1-6, only incident photons with energy higher than the band gap energy of the absorber layer can excite charge carriers and generate electron-hole pairs. And since the electrons tend to fill energy levels at the bottom of the conduction band and the holes fill energy levels at the top of the valence band. Therefore, if there is extra energy that the electron-hole pairs receive from the photons, it is eventually released as heat into the semiconductor in the thermalisation process. On the other hand, incident photons with energy lower than the band gap energy of the semiconductor absorber are not absorbed and cannot participate in electron-hole pairs' generation. Therefore, these photons are not involved in the energy conversion process. As a result, the excess energy of photons, larger than the band gap and the non-absorption of photons carrying less energy than the semiconductor band gap are considered in S-Q limit together with the radiative recombination. Therefore, S-Q limit gives a maximum efficiency of 33.7% of a single p-n junction using a semiconductor material with 1.4 eV band gap and AM1.5 solar spectrum.

In Figure 1-10, the values of power conversion efficiency as function of band gap for several important solar cell materials are shown. The ultimate efficiency is determined by the absorption edge and thermalization of excited electrons. The nominal efficiency, which is always lower than the ultimate efficiency, is a result of radiative recombination of electrons and holes. The detailed-balance limit of efficiency is a fundamental limit for the conditions considered by Shockley and Queisser.

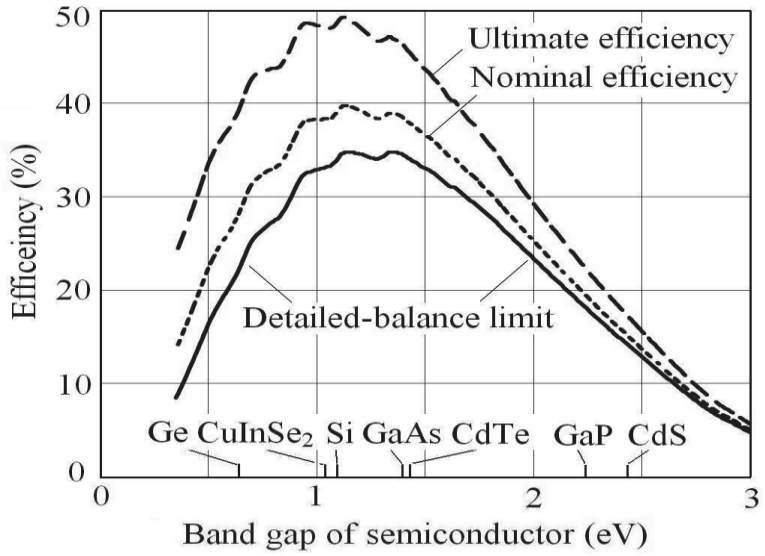

Figure 1-10: Efficiency limit of solar cells for AM1.5 solar radiation. Efficiency limit as determined by detailed balance. The solar radiation is approximated by blackbody radiation at 5800 K [24].

Some design rules can be used to allow for passing the Shockley Queisser limit, such as use more than one semiconductor material with more than one band gab, often referred to as a multi-junctions or tandem cells, to reduce the amount of excess energy.

Other losses such as surface reflection, non-ideal blackbody solar cells and Auger and SRH recombination can also limit the production of the solar cells.

1.2.6: Solar Cells Parameters

It is known that a solar cell can be modeled by a current source connected in parallel with a p-n junction diode. Figure 1-11 shows a typical solar cell consisting of internal parasitic shunt resistance, R_{shunt} and series resistance R_{series} .

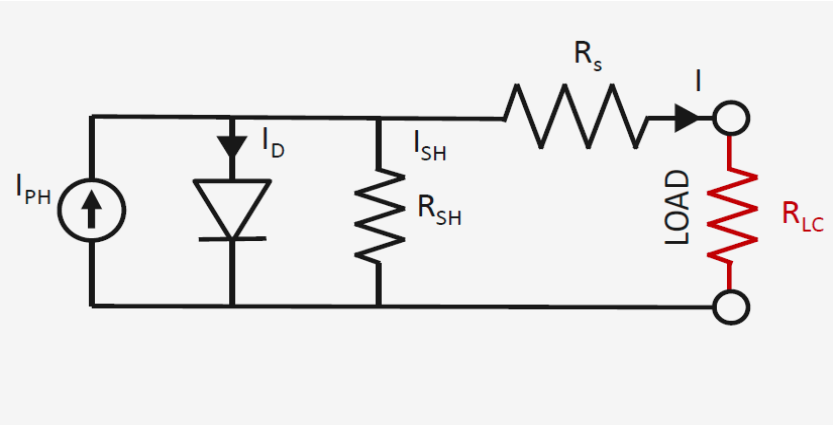

Figure 1-11: A solar cell circuit with series and shunting resistances [22].

The performance of solar cells is characterized by *I-V* measurements, which is shown in Figure 1-12 for a typical solar cell under illumination. The important parameters are the short-circuit current (I_{SC}), open-circuit voltage (V_{OC}), fill factor (*FF*), and energy conversion efficiency (η).

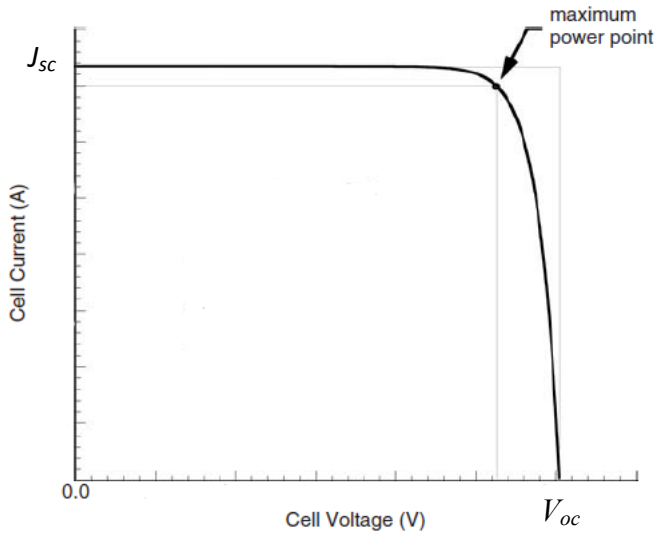

Figure 1-12: A typical current–voltage characteristic curve under illumination [22].

In the dark, the solar cell behaves as a diode with a current:

$$I_D = I_0 \left[\exp\left(\frac{q(V+IR_s)}{nkT}\right) - 1\right] + \frac{V+IR_s}{R_{sh}} \quad (1\text{-}7)$$

where I_0 is reverse saturation current, and n is the diode factor.

Under the illumination, the net current is given by:

$$I = I_{PH} - I_D = I_{PH} - I_0 \left[\exp\left(\frac{q(V+IR_s)}{nkT}\right) - 1\right] - \frac{V+IR_s}{R_{sh}} \quad (1\text{-}8)$$

where I_{pH} is the photo-generated current.

The short-circuit current (I_{SC}) is the current that flows through the external circuit when the electrodes of the solar cell are short circuited. It depends on the photon flux density incident on the solar cell, which is determined by the incident light spectrum. Typically, the global standard spectrum is the 1.5 AM spectrum.

The I_{SC} is corresponded to the current at $V = 0$, and given by:

$$I_{SC} = I_{PH} - I_0 \left[\exp\left(\frac{q(IR_s)}{nkT}\right) - 1\right] - \frac{IR_s}{R_{sh}} \quad (1\text{-}9)$$

Usually, the short-circuit current density J_{sc} is used to describe the maximum current delivered by a solar cell in order to remove the dependence of the solar cell area.

The maximum current that the solar cell can generate is strongly depends on the optical properties of the solar cell, such as absorption and reflection parameters.

Next parameter is the open-circuit voltage V_{OC} which is considered when no current is flowing through the cell, *I=0*, and it can be given by:

$$V_{OC} = \frac{nkT}{q} \ln\left(\frac{I_{PH}}{I_0} + 1\right) \quad (1\text{-}10)$$

It is obvious from this equation that the V_{oc} depends on the saturation current of the solar cell and the photo generated current. Typically, the saturation current I_o depends on the recombination in the solar cell. Therefore, V_{oc} is strongly depends on the amount of recombination in solar cell device.

Another parameter is the fill factor (FF), which is given by dividing the maximum power P_{max} over the theoretical power output P_T :

$$FF = \frac{P_{max}}{P_T} = \frac{(I_{max} \times V_{max})}{(I_{SC} \times V_{OC})} \quad (1\text{-}11)$$

The conversion efficiency is given by the ratio of the output electrical power P_{out} , to the input power P_{in} :

$$\eta = \frac{P_{out}}{P_{in}} = \frac{(I_{SC} \times V_{OC} \times FF)}{P_{in}} \quad (1\text{-}12)$$

Furthermore, the shunt resistance is resulted from the defects of the crystal structure, which provide alternative paths for the current to flow. The series resistance is caused by the semiconductor-metal contacts at both electrodes, which contain a resistivity for the current flow. Ideally and for high solar cells performance, it is required to make the shunt resistance as big as possible, infinity, to reduce a lockage current, and the series resistance as small as possible, Zero, to collect more current. The effect of series and shunt resistance is shown in Figure 1-13.

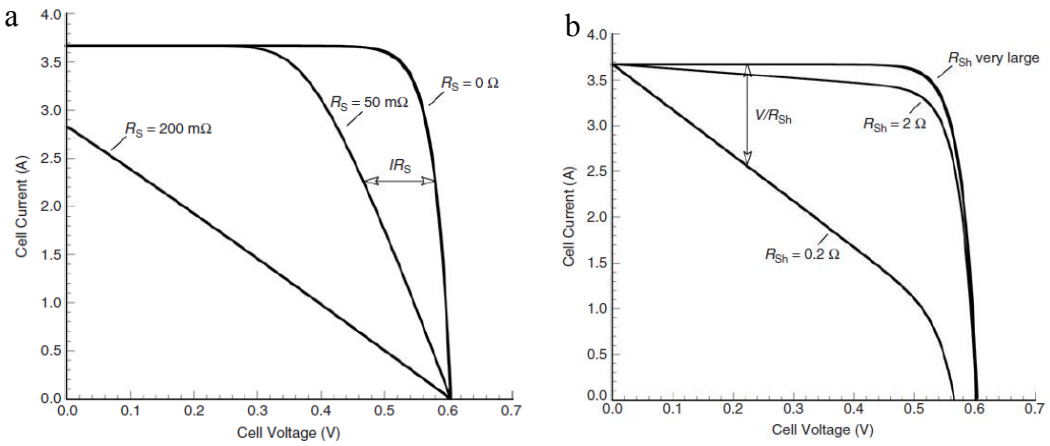

Figure 1-13: Effect of series resistance at ($R_{sh}\rightarrow\infty$) (a) and shunt resistance at (R_s=0) (b) on the current–voltage characteristic of a solar cell [22].

1.2.7: Charge Carrier Recombination

Another important concept in solar cells is the charge carrier recombination, which is crucial to solar cell performance. A non-equilibrium state is created due to the generation of charge carriers and therefore recombination processes seek to reach equilibrium. When a photon is absorbed and an electron-hole pair is generated, they have to be swept across the junction before they recombine. Moreover, there are several mechanisms that are responsible for recombination which can be shown in Figure 1-14. One recombination process is called Auger recombination in which the energy released during recombination is given to another carrier and then released as a phonon mode. Phonon mode causes a lattice vibration and is nothing different than heat. Therefore, Auger recombination becomes dominant in photovoltaic materials with high densities of charge carriers, like in highly doped Si. Another recombination process is radioactive recombination or band-to-band recombination which is the reverse process of optical generation where electrons drop from the conduction band to the valence band and emit photons.

Also, recombination can occur through traps (defects) with energies located in the bandgap. This is called Shockley-Read-Hall (SRH) recombination. The electron is trapped until a mobile hole finds the electron and both charge carriers recombine.

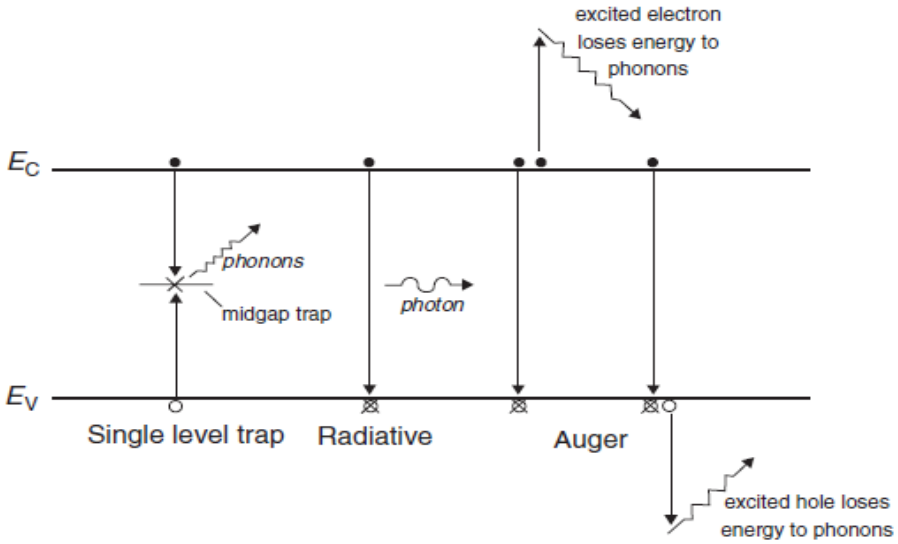

Figure 1-14: Recombination processes in semiconductors [22].

The minority charge carrier lifetime τ_0 is dependent on the defect density N_t on the following expression:

$$\tau_0 = {N_t}^{-1} \tag{1-13}$$

And the open circuit voltage can by written as:

$$V_{oc} = \frac{2kT}{q} \ln\left(\frac{G_L \tau_0}{n_i}\right) \tag{1-14}$$

Where G is the generation rate, and n_i is the intrinsic density of the charge carriers of the semiconductor material.

Therefore, it is obvious that the larger the defect density, the shorter the life time of the minority of charge carrier and the smaller the open circuit voltage. Defects can be located in the bulk of the semiconductor materials, and also can be present at the interfaces between materials or the metallic contacts used in the solar cell. Recombination mechanisms in CdTe solar cells are typically dominated by SRH recombination [25, 26].

1.3: Basics of Thin Film Solar Cells

1.3.1: Thin Film Properties

Silicon has been widely used for solar cells manufacturing. However, it has some disadvantages, such as its indirect band gap which makes the absorption coefficient near its band edge is low. Therefore, a fairly thick substrate is required. Usually, the minimum thickness to obtain reasonable absorption and mechanical strength is 0.1 – 0.2 mm, which is one of the reasons for high material and manufacturing cost. On the other hand, the direct semiconductors often have absorption coefficient one or two orders of magnitude higher than silicon as it is shown in Table 1-1[22].

Table 1-1: Properties of common solar cell materials.

Material	Ge	$CuInSe_2$	Si	GaAs	CdTe
Type	Indirect	Direct	Indirect	Direct	Direct
Band gap (eV)	0.67	1.04	1.11	1.43	1.49
Absorption edge (μm)	1.85	1.19	1.12	0.87	0.83
Absorption coef. (cm^{-1})	5.0×10^4	1.0×10^5	1.0×10^3	1.5×10^4	3.0×10^4

For those materials, with direct band gap, a thickness of a few micrometers is enough to absorb most of incident light. In addition to a high absorption coefficient near the band gap, there

are many other factors which determine the practicality of making a solar cell, such as fabrication methods, life time, availability and stability. Nowadays, there are only two such materials besides silicon have reached the status of mass production. These materials are cadmium telluride (CdTe) and copper indium-gallium diselenade, $Cu(InGe)Se_2$, which often called CIGS. Both of them have a direct band gap and high absorption coefficient, and therefore they are very desirable for thin film applications.

1.3.2: CdTe-Thin Film Solar Cells

In this section we will discuss the thin-film cadmium telluride (CdTe) technology which is one of the low cost materials for photovoltaic applications. Over the past several decades, CdTe thin-film technology has grown significantly. Figure 1-15 shows record of solar cell efficiencies of CdTe and other leading solar cell technologies since the 1970's[27]. The record conversion efficiency of lab-scale solar CdTe solar cells, which was obtained by GE Global Research in 2013, is 19.6% and recently 21% by First Solar [28].

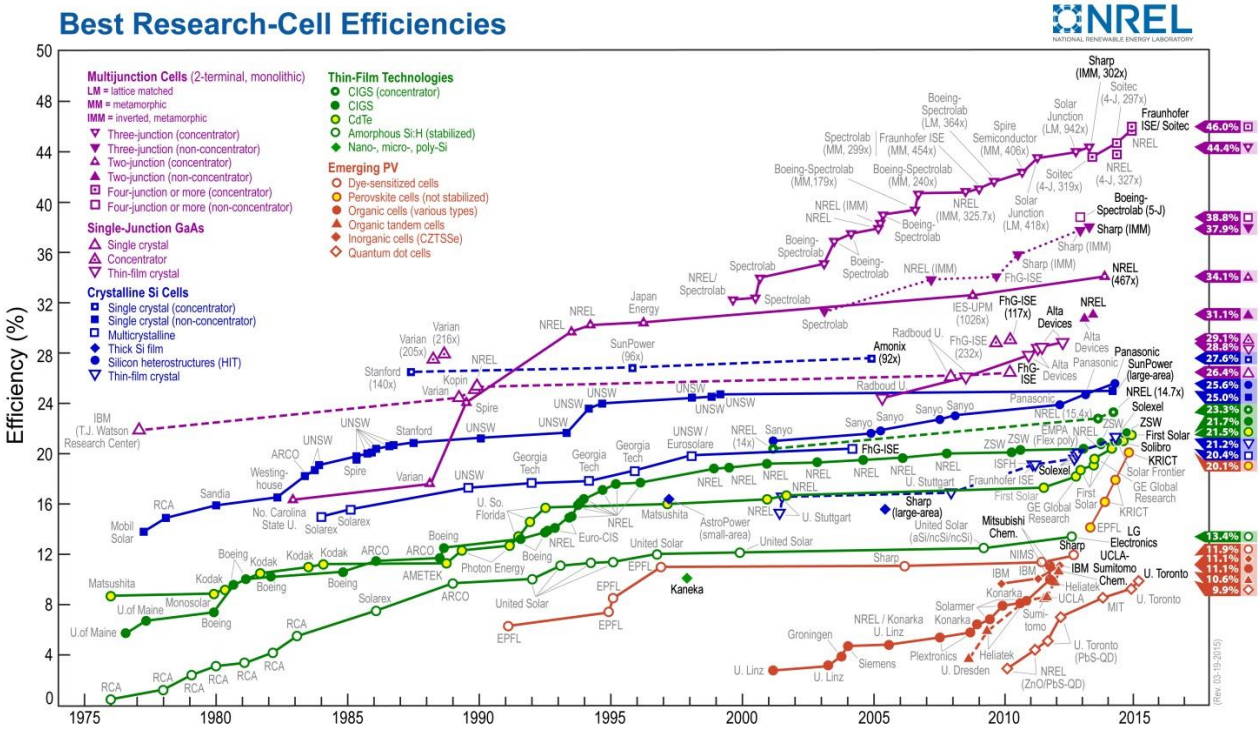

Figure 1-15: Record solar cell efficiencies over the past 40 years [27].

CdTe is an II-VI semiconductor because it consists of the II valence electron element cadmium (Cd) and the VI valence electron element tellurium (Te). The lattice structure of CdTe forms is a zinc-blende where every Cd atom is bonded to four Te atoms and vice versa. The band gap of CdTe is ~1.5 eV, which is matched the optimal solar spectrum range. It has a direct band gap, consequently only a small thickness of CdTe is required to absorb all the photons with energy higher than the band gap energy. These properties together with its high absorption coefficient of 10^4- 10^5 cm^{-1} make it very desirable material for thin film technology. Another advantage of CdTe is its compatibility with n–type CdS, which is a wide-band-gap semiconductor (~ 2.4 μm) for which it is a good transparent to the bulk of solar radiation.

Typically, the CdS layer is made as thin as possible to allow the maximum number of photons to pass through to the CdTe layer.

In solar cells, p-doped CdTe is used, which can be obtained by replacing Cd with an I-valence electron atom like copper, silver or gold. Also, it can be achieved by replacing Te-atoms with V-valence electron elements such as nitrogen, phosphorus or arsenicum. In Figure 1-16, the structure of a typical superstrate configuration of CdTe solar cells is shown.

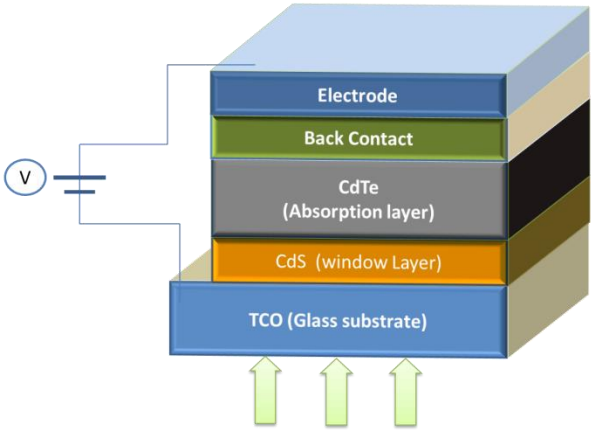

Figure 1-16: A typical superstrate configuration of CdTe solar cells.

1.3.3: Deposition Methods

Many methods have been used to deposit CdTe thin films for solar cells. Among them, there are eight methods that have been widely used in the commercial manufacture of CdTe solar cells and modules over the past decade. These methods together with their temperature and pressure conditions, film thickness and growth rate are summarized in Figure 1-17.

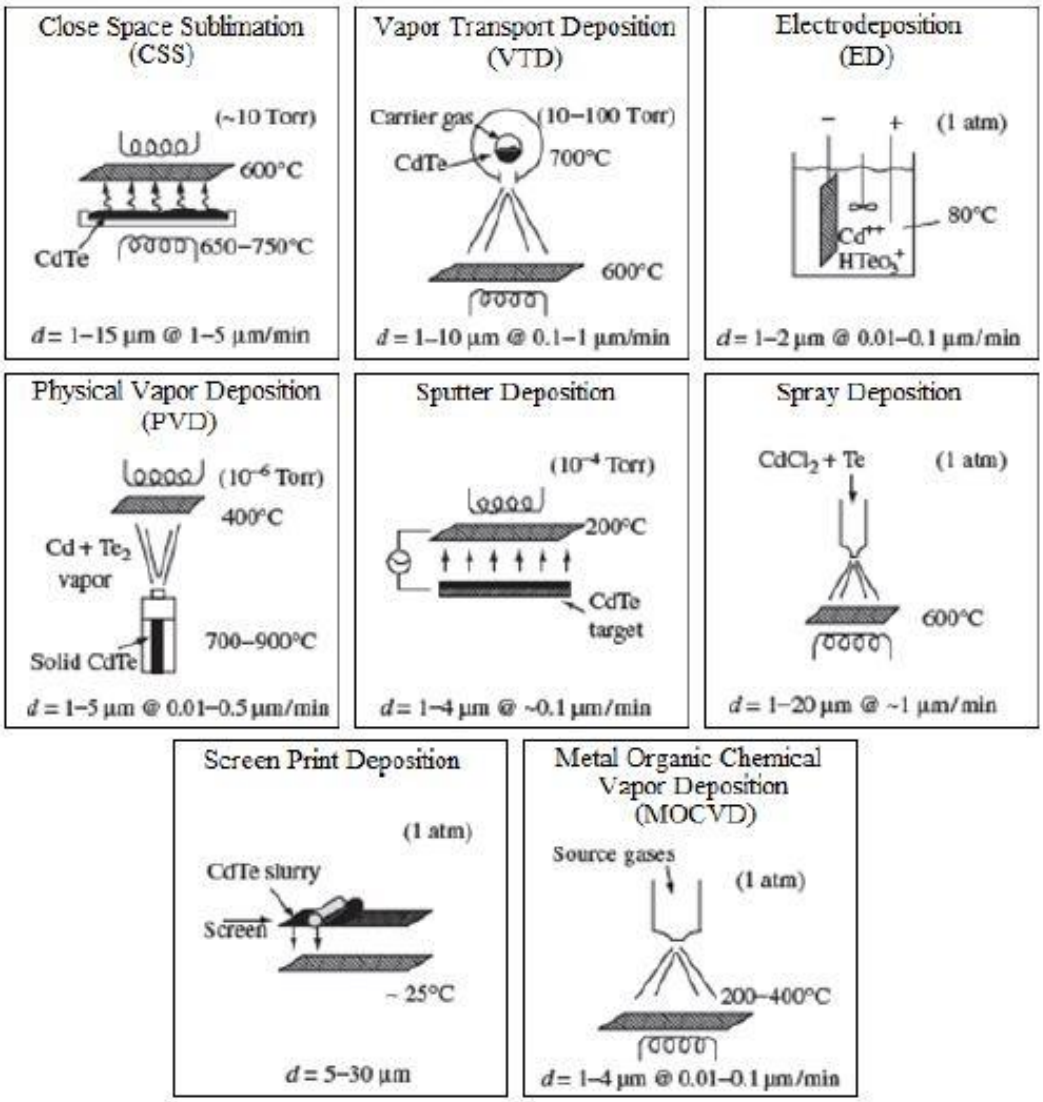

Figure 1-17: CdTe thin-film deposition techniques. The substrate in each view is the cross-lined rectangle. Film thickness (d) and growth rate are shown at the bottom of each figure [25].

The closed space sublimation (CSS) method has proved to be very effective, and it has produced solar cells with the highest efficiencies [29]. In this method, the source and the substrate are placed at a few millimeters up to several centimeters from each other under vacuum conditions. The source can either consists of granulates or powders of CdTe. The substrate is

heated up to 600 ^{0}C, and the source is kept at a higher temperature than the substrate to generate a temperature difference, which induces a driven force on the precursors to deposit it on the substrate. This process is used under an inert gas like argon or nitrogen. Typical thicknesses for CdTe films are ~3-8 μm and CdS layers are ~120 nm thickness. Further, in this work, another deposition method has been used, which is known as pulsed laser deposition, to deposit both CdS and CdTe layers at low temperature ~ 200 ^{0}C. This method and its advantages will be presented in the next chapter.

1.3.4: Challenges and Motivations

From what has been stated in thin film based solar cells discussion, it is obvious that thin film for solar cells and other photovoltaic applications is very desirable and challenging at the same time. One challenge is to fabricate thin film CdS/CdTe using low deposition temperature which is very beneficial for achieving a precise control of the CdS/CdTe microstructure and optoelectronic properties. Also, low temperatures provide benefits in wider selection of substrates especially those for low-cost, flexible solar cells applications, so it is desirable for industrial purposes. However, thin films CdTe fabricated in such low temperatures are usually suffering from many defects and structural pin-holes. Therefore, many efforts have been made to obtain highly crystalline thin films by using *ex situ* $CdCl_2$ treatments which proved to be very useful treatments to get high performance solar cells.

In this work, thin films CdTe based solar cells has been fabricated in two different thicknesses of 1.3 μm and 0.75 μm by using pulse laser deposition method at low temperature of 200 ^{0}C. A new *In situ* Thermal Annealing Process (iTAP) has been developed as an additional

process before the *ex situ* $CdCl_2$ treatments to get highly crystalline thin film structure by controlling the microstructural and crystallinity properties of CdS/CdTe thin film solar cells. Significant improvement in microstructure and crystallinity of CdTe thin films has been obtained in optimal iTAP processing window, which leads to improved solar cell performance including J_{sc}, V_{oc}, *FF*, QE, and overall efficiency. These improvements suggest that the iTAP process could provide a robust method in controlling the crystallinity and microstructure of CdTe thin film solar cells.

Chapter 2 : Experiment

In this chapter, a description of the fabrication steps of the solar cells devices will be presented together with an overview of all the measurements that have been used to study different properties. For example, the morphology properties were studied by using Atomic Force Microscopy (AFM). Then, Raman Spectroscopy (RS) was used to figure out the structural properties. Optical properties were studied using transmission and band gap measurements. Overall performance was tested by current density-voltage (*J-V*) measurements. And other physical characterization was done by using quantum efficiency (QE) analysis. The thickness of the films was measured by probe surface profile-meter (KLA-Tencor P.16). The results from these selected measurements are studied and compared with changes in processing conditions. All The fabrication and measurement steps were carried out in the Nanotechnology-Thin Film laboratories at the University of Kansas, in the USA.

2.1: CdS/CdTe Thin Film Fabrication Process

In order to fabricate a CdS/CdTe solar cell device, the process should go through many steps for different purposes as it is summarized in Figure 2-1. The following sections will discuss these steps in details.

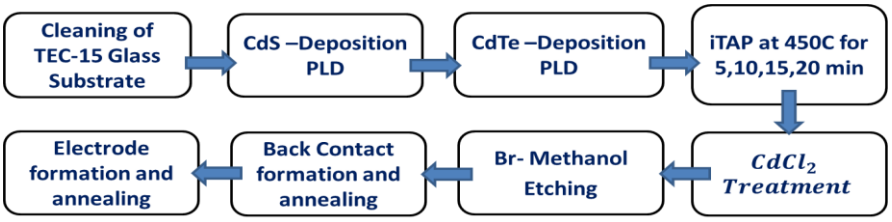

Figure 2-1: Fabrication progress of CdTe thin film based solar cells.

2.1.1: Pulse Laser Deposition Method of CdS/CdTe Layers

Tec-15 glass substrate coated with a transparent conductive oxide (TCO) layer was cleaned using acetone, methanol and DI-water, and used as a front contact of all the devices. The standard PLD method [30] was used to fabricate both the window and absorption layers of our solar cells devices by using a German Lambda Physic KrF laser of wavelength $\lambda = 248$ nm, and a multi-port stainless steel vacuum chamber equipped with a gas entry as it is shown in Figure 2-2.

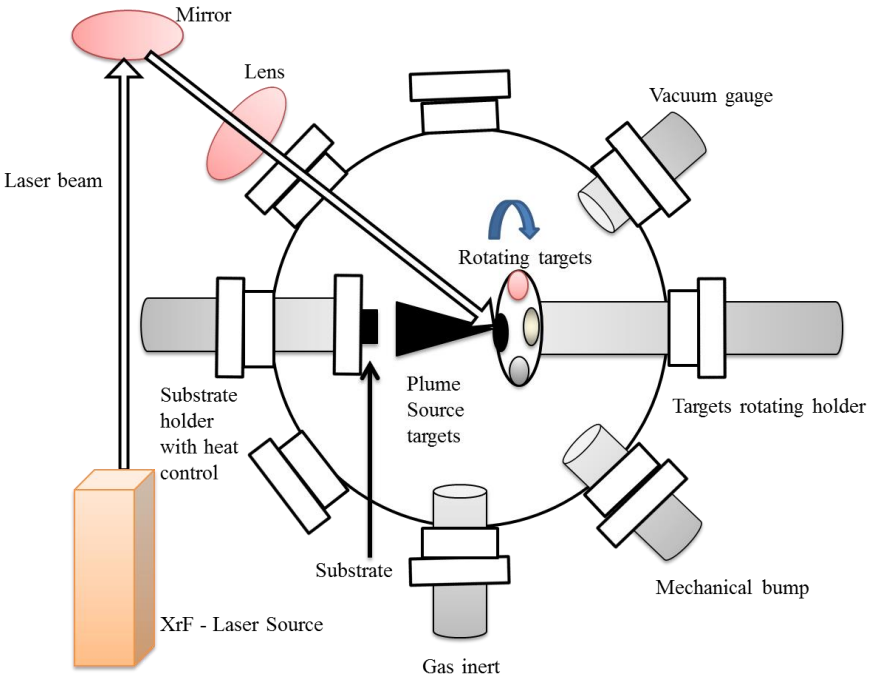

Figure 2-2: PLD setup system.

In this work, the pressure inside the chamber reached at less 5×10^{-6} mTorr and the deposition of CdS and CdTe thin films was conducted under an argon atmosphere of ~1.5 mTorr to avoid material loss. The substrate holder was fitted with a resistive heater to control and maintain the substrate temperature at the desired value during the deposition and iTAP. Both CdS and CdTe targets (purity 99.99 at. %) were installed at a distance of 5.5 cm from the substrate on a rotated holder to provide an ability to choose a desired target. The targets were

also rotating at 30 rpm during the deposition to avoid fast drilling. The laser energy densities used for the incident laser beam were 0.7 and 0.6 J/cm^2 at the CdTe and CdS surfaces, respectively, with a 10 Hz of repetition rate. The laser beam was focused on the target surface with a ~4 cm focal length lens in front of the vacuum chamber at an angle of 45^0, with respect to the normal. The substrate temperature was constant at 200 ^{0}C. The PLD system that was used in this work at the University of Kansas, Department of physics and Astronomy is shown in Figure 2-3.

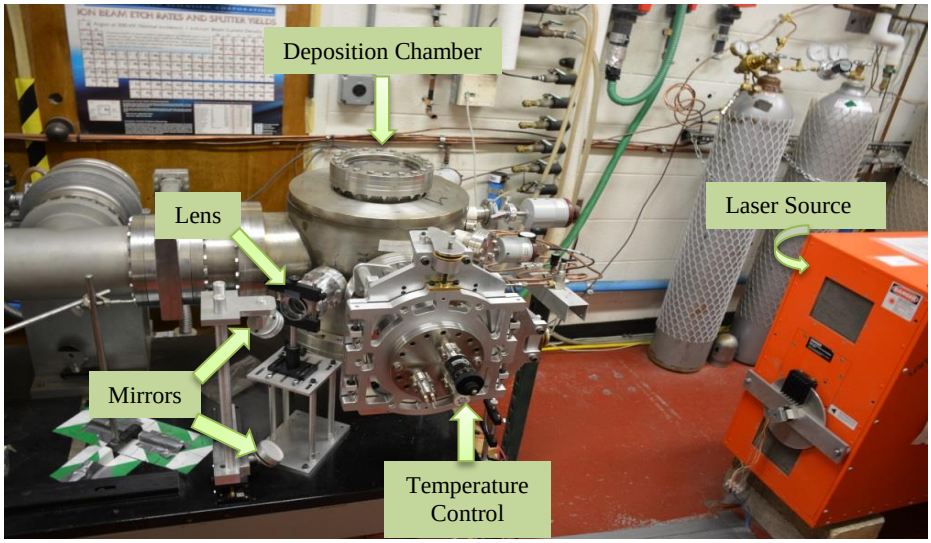

Figure 2-3: PLD system at the University of Kansas.

2.1.2: *In situ* Thermal Annealing Process (iTAP)

Using low PLD deposition temperature of 200 ^{0}C for both CdS and CdTe layers is very beneficial to obtain a precise control of the CdS/CdTe microstructure and optoelectronic properties. However, the CdS/CdTe solar cells based on thin CdTe films fabricated at low temperature have generally poor performance as a result of increased density of grain boundaries and defects. Therefore and to address this issue, an *in situ* thermal annealing process (iTAP) has

been applied immediately after the CdS/CdTe deposition and before the common *ex situ* $CdCl_2$ annealing typically employed for optimization of the CdTe-based solar cells. Four samples are subjected to iTAP at 450 ^{0}C for different durations as can be seen in the temperature diagram in Figure 2-4.

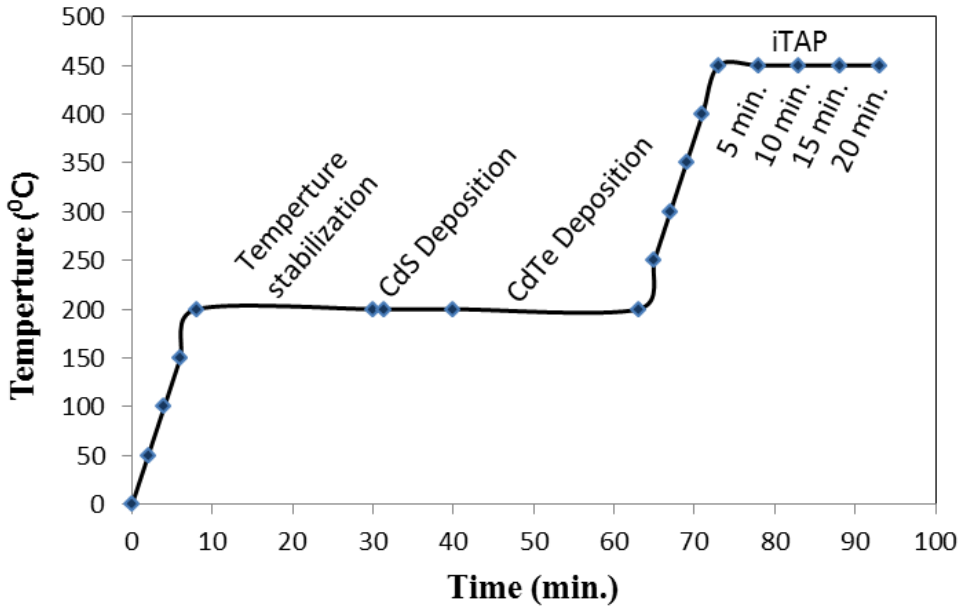

Figure 2-4: Deposition and iTAP temperature diagram.

The temperature was raised gradually reaching the deposition temperature of 200 ^{0}C in 8 min., and was kept for around 20 min. to reach a stabilized point. Then, CdS and CdTe depositions were completed at this temperature and ~1.5 mTorr Argon. After the deposition and to apply iTAP, the temperature was increased up to 450 ^{0}C in 10 min and the Argon pressure to 20 Torr. The samples were annealed under this temperature for durations of 5, 10, 15, 20 min. The samples then left inside the chamber until next day to cool down after dismissing temperature source. After that, AFM and Raman spectra were carried out by using WI-Tec

AFM-Raman system, which will be discussed later, to study the change of the morphology and crystal structures of all samples.

2.1.3: $CdCl_2$ Treatment

The $CdCl_2$ treatment was assigned to the samples after the iTAP and AFM-Raman measurements. The $CdCl_2$ source was made from the saturated $CdCl_2$ methanol solution by dropping it onto a cleaned glass that was under heating at 100 ^{0}C in order to evaporate the methanol and leave the $CdCl_2$ on the glass. Then, to do the treatment process, the samples were flipped to face the dry $CdCl_2$ source and separated them by small class masks as it is shown in Figure 2-5. Finally, samples were placed in a furnace tube and treated them at 360 ^{0}C for 15 min with a flow of Ar (100 sccm) and O_2 (25 sccm). This process is very important to improve solar cells performance by increasing the p-CdTe doping, reducing grain boundaries and blocking channel pinholes.

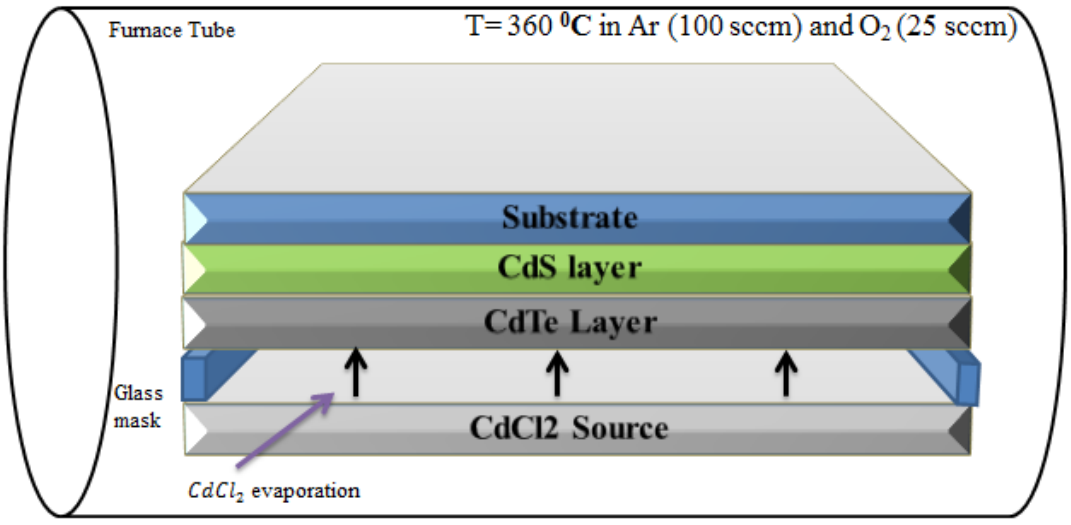

Figure 2-5: $CdCl_2$ treatment setup.

2.1.4: Bromine Etching

This step was carried out after $CdCl_2$ treatment in order to remove the $CdCl_2$ residues on the surface of the films and make it Te-rich. It was done by placing the films into a mixing solution of 0.1 mL Br and 100 mL methanol for 4 seconds, and then samples were rinsed directly in methanol, acetone and DI-water.

2.1.5: Back Contact and Silver Electrode Formation

The *HgTe:Cu* doped *graphite* paste is the slandered back contact was used in this work. It gives a good back contact resulting in good performance by providing high work function and increasing CdTe doping. The *HgTe:Cu:graphite* paste was dropped onto the CdTe surface to form 30 solar cells total on each film. The annealing of the back contact was performed by placing the device in a tube furnace at 280 ^{0}C for 30 min in a 100 sccm Ar flow. After that, an electrode, Ag, paste was dropped on the back contact, and then an electrode annealing took place by placing the device in a tube furnace at 100 ^{0}C for 60 min. Finally, the final superstrate configuration of the fabricated solar cell can be seen in Figure 2-6.

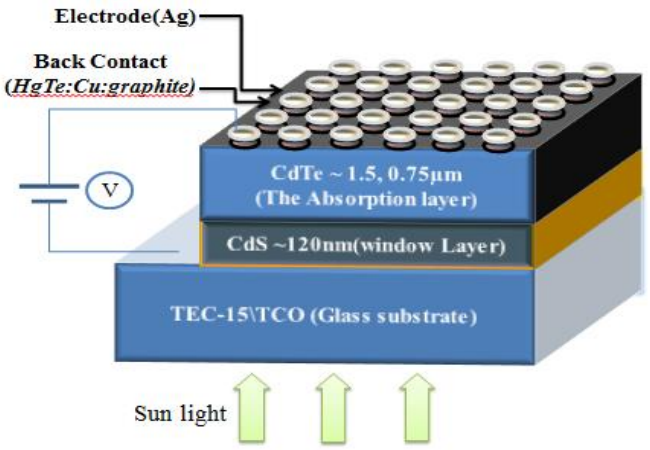

Figure 2-6: Superstrate configuration of the fabricated solar cells.

2.2: Atomic Force Microscopy (AFM)

Atomic force microscopy (AFM) is a technique that has been used to investigate and study the surface topography as well as surface roughness of materials. It uses a very tiny probe with a tip radius of several nanometers to scan the surface of a sample, as it is shown in Figure 2-7 and 2-8b [31]. The probe is located at the end of a cantilever and they are typically made from silicon, silicon oxide, or silicon nitride [32]. When the probe with a tip are brought so close to the surface, the atomic forces between the surface and the probe become important and play a role in determining surface morphology.

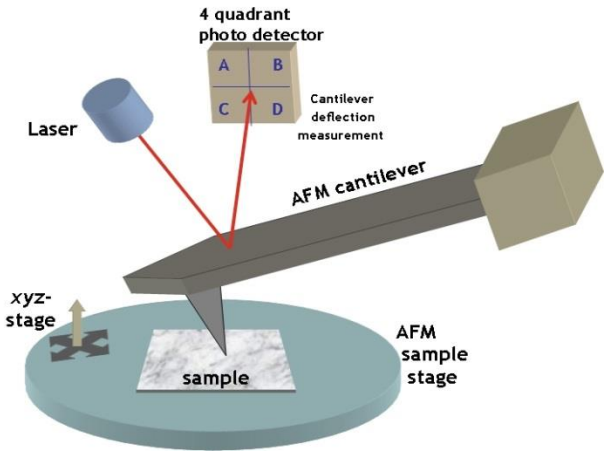

Figure 2-7: A typical diagram of an AFM setup [31].

Typically, AFM setup is designed in two different ways to monitor the motion of the cantilever. In one way, the sample is moved and the cantilever is fixed. In another way, the cantilever is scanned over the stationary sample, which is the common way. When the cantilever scans across the sample, laser beam is focused at the back of the cantilever that is made of a reflective layer of gold or aluminum. The laser is reflected to different positions on a photodiode due to the moving probe, and therefore this data is recorded to create a picture of the scanned sample.

There are different techniques that can be used for the cantilever to be scanned across the surface. One scanned method is what so called a non-contact mode, in which the tip does not contact the surface but depends on van der Waals forces to displace the cantilever. And since the van der Waal interaction is very weak, the tip must be oscillated to detect surface topography and results in low resolution mapping. Another scanned technique is called the contact mode, in which the tip is basically contacted and dragged across the surface of the sample. This technique is not preferable for some types of samples in which the dragging of the tip can lead to tip or sample damage. Another method that combines contact and non-contact modes is called the tapping mode, in which the cantilever is oscillated near its natural frequency. The amplitude of oscillation reduces when it comes into contact with the sample surface, and the sample height is adjusted to obtain constant amplitude and can be used to obtain an image of the surface.

In our work, we used a WI-tech system AFM, which is shown in figure 2-8 [33] to study the morphology properties, using scan mode in which the cantilever is scanned over the stationary sample in contact mode.

Figure 2-8: a) WI-Tech AFM-Raman system, b) AFM probe and tip [33].

2.3: Raman Spectroscopy (RS)

Raman spectroscopy (RS) is a very powerful spectroscopic technique based on inelastic scattering of monochromatic light that is usually provided by a laser source. Inelastic scattering can be defined based on the change of frequency of photons in monochromatic light as a result of interaction with a sample [34]. When the laser light incident on the sample, photons are absorbed and then reemitted by the sample. The reemitted photons' frequency is shifted up or down in comparison with original monochromatic frequency, this is called the Raman Effect. This shift in frequency provides important information about vibrational, rotational and other low frequency transitions in molecules. Therefore, RS can be used to investigate solid, liquid and gaseous samples.

The Raman Effect is understood based on molecular deformations in electric field E that is determined by molecular polarizability α. In this effect, the laser beam can be considered as an oscillating electromagnetic wave with electrical vector E. As a result of the interaction of this laser beam with the sample, it produces electric dipole moment P = αE which deforms molecules. Because of periodical deformation, molecules start vibrating with amplitude that is called a nuclear displacement, and new frequency υ_M. In other words, the incident monochromatic laser light with frequency υ_0 excites molecules and transforms them into oscillating dipoles [34]. These oscillating dipoles emit light in three different ways with different frequencies as shown in Figure 2-9.

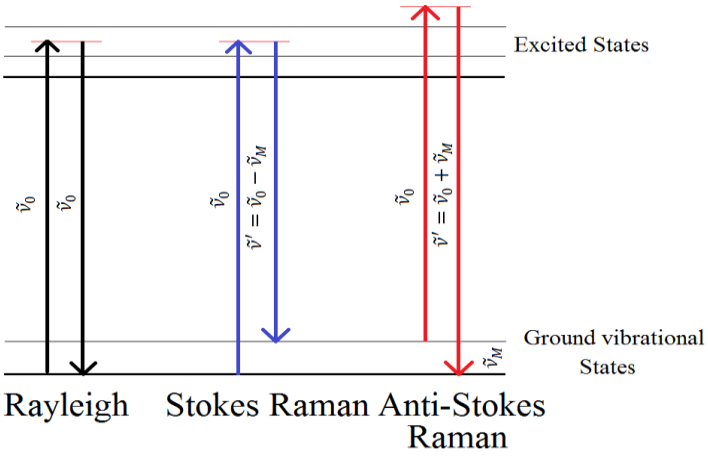

Figure 2-9: Principle of Raman Spectroscopy [35].

First, if the excited molecule returns back to the same basic vibrational state and the emitted light has the same frequency υ_0 as an excitation source, this type of interaction is called an elastic Rayleigh scattering. The molecule in this case has no Raman-active modes.

Second case, a photon with frequency υ_0 is absorbed by Raman-active molecule which is in the basic vibrational state at the time of interaction. Part of the photon's energy is transferred to the Raman-active mode with frequency υ_M and the resulting frequency of scattered light is reduced to υ_0- υ_M. This Raman frequency is called Stokes frequency.

Third case, a photon with frequency υ_0 is absorbed by a Raman-active molecule which is already in the excited vibrational state at the time of interaction. In this interaction, excessive energy of excited Raman active mode is released, molecule returns to the basic vibrational state and the resulting frequency of scattered light goes up to υ_0 + υ_M. This Raman frequency is called Anti-Stokes frequency.

In measurements setup, a Raman system typically consists of four major components which are excitation source laser, illumination system and light collection optics, wavelength

selector, and detector. In our measurements, the Raman spectra were detected by using WI-Tec AFM-Raman system shown in Figure 2-8, which focuses its wavelength laser beam (λ_{exc} = 488 nm) with a spot-size of about 2 μm onto the sample. Results analyses were studied based on the selection rules of CdTe corresponding peaks.

2.4: Transmittance and Band Gap Measurements

The optical properties of the CdTe thin films fabricated under different TAP conditions were studied by measuring transmission of light at each wavelength and bang gap values. The CdTe thin film transmissions of photons have lower energy than the band edge of CdTe is an essential property to study and detect the defects and interband levels in crystal structure. The transmittance can be defined as the ratio of the transmitted radiant energy to incident radiant energy, or the fraction of the light that pass through a material. It can be described as:

$$\mathrm{T}\ (\%) = \frac{Transsmited\ light}{Incident\ light} \tag{2-1}$$

The band gap of CdTe can be estimated by using the following Tauc equation [36]:

$$\alpha = \frac{k}{hv}(hv - E_g)^{n/2} \tag{2-2}$$

Where *k* is a constant, *n* is a constant that equal to 1 for direct gap material such as CdTe. α is the optical absorption coefficient that can be calculated by using Beer-Lambert Law:

$$I = I_0 \exp(-\alpha t) \tag{2-3}$$

Where I and I_0 are the transmitted and incident radiation intensities, and t is the thickness. Thus, CdTe band gap is approximated from the $(\alpha hv)^2$ against hv plots by extrapolating the straight-line portion over the hv axis.

Optical transmittance of the films was characterized by UV–Vis–NIR spectrophotometer (PerkinElmer Lambda 950), within the spectral range of 300–900 nm.

2.5: Current Density-Voltage Measurements (*J-V*)

Current density-voltage measurement is one of the most principle methods of characterizing the electrical properties and performance of solar cells. The *J-V* testing is carried out by measuring the cell fill factor, open circuit voltage, short circuit current density, and efficiency. The mathematical formulas are already described in chapter 1.2.6. A typical *J-V* measurements setup consists of an electric circuit connected in series to a power supply and an ammeter and a voltmeter. In our solar cell laboratory at the University of Kansas, the electrical properties of prepared solar cells were measured by using a CHI660D electrochemical workstation, a solar simulator at 1.5 AM and a Newport 69911 spectrometer. This setup consists of a high resolution camera that used to easily made connection with the front and back contacts of the cell using tiny tips. The power supply, voltmeter, and ammeter are connected with a computer equipped with data acquisition software.

The cells under dark and sun light illumination conditions are subjected to a range of voltages that are usually in the range of -0.5 V to 1 V. A standard light spectrum with an air-mass (1.5 A.M) and intensity of (~100 mW/cm^2) are used to characterize solar cells. Then, data analysis was obtained by using python programing code.

2.6: Quantum Efficiency (QE)

The Quantum efficiency QE measurement is one of the most powerful characterization techniques for solar cells. It can be defined as the amount of photons incident on the solar cell that create electron-hole pairs in the absorber layer which are successfully collected. QE can be described by two types which are external and internal. The QE measured in this study is external QE that is resulted from all the effects that occur externally to the cell. Internal QE only considers photons that are incident on the junction of the device, and therefore it is higher than the external QE value. The QE of a typical silicon solar cell is shown in Figure 2-10.

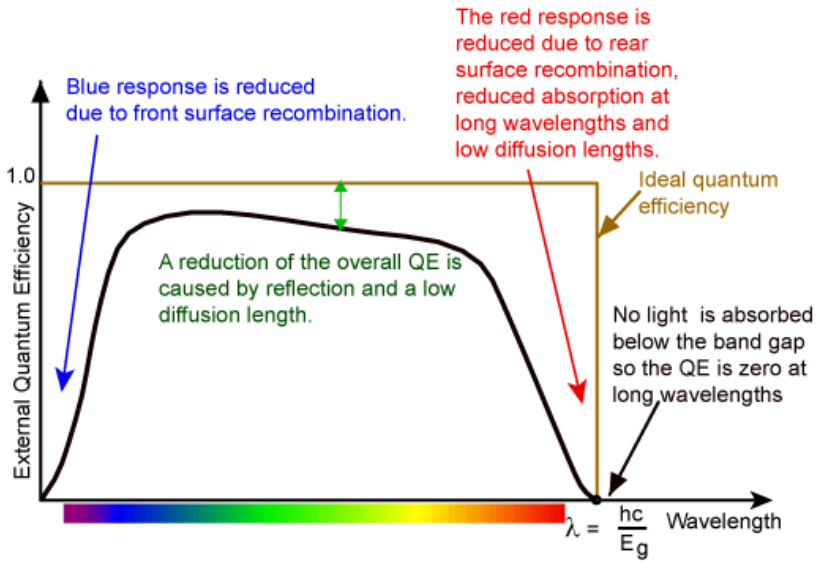

Figure 2-10: QE of a typical silicon solar cell [37].

QE depends on the incident wavelengths, and it is measured usually by illuminating the solar cell with monochromatic light of wavelength λ_0 and recording the photocurrent I_{ph} through the solar cell. Thus, QE can be given by:

$$\text{QE}\ (\lambda_0) = \frac{\text{Number of collected electrons}}{\text{Number of incident photons}} \qquad (2\text{-}4)$$

Or

$$\text{QE}\ (\lambda_0) = \frac{I_{ph}(\lambda_0)}{\mathrm{q}\ \phi_{ph}\ (\lambda_0)} \tag{2-5}$$

Where q is the elementary charge and ϕ_{ph} is the incident photon flux.

QE spectra are measured using a QE-setup that is shown in Figure 2-11. It is also called spectral response setup. In this measurement, it is usually required to have a wavelength selective light source, a calibrated light detector and a current meter. The typical used light source is a xenon gas discharge lamp that has a very broad spectrum covering all the powerful wavelengths for the solar cell performance. A very narrow wavelength band of incident photon energies can be obtained by using filter and monochromator.

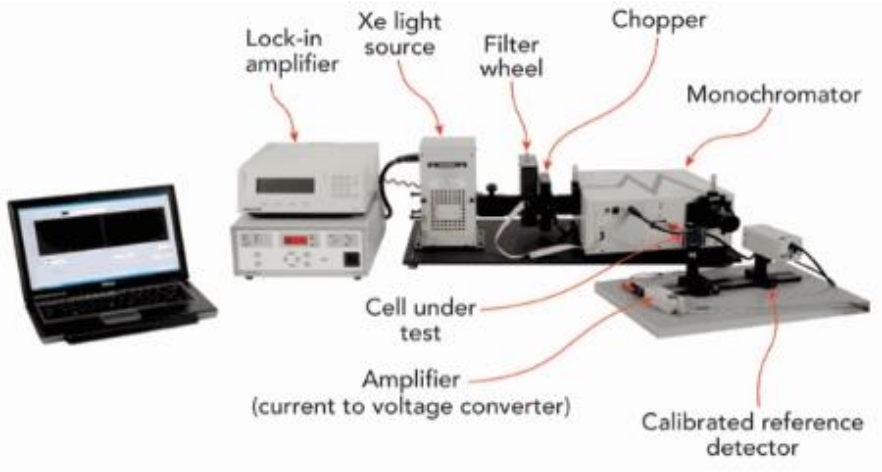

Figure 2-11: Typical setup for QE measurement [38].

Chapter 3 : Effect of *In Situ* Thermal Annealing Process on Structural, Optical and Electrical Properties of CdS\CdTe Thin-Film Solar Cells

In this work and by using the fabrication steps that were already described in chapter 2, two different sets of solar cells devices were fabricated in superstrate configuration in the same CdS thickness (120 nm) and different CdTe thickness. The first set have a CdTe thickness of 1.3 µm, while the other set have a CdTe thickness of 0.75 µm. Both sets consist of five samples with 30 solar cells on each sample. The thickness of the layers was measured by using probe surface profile-meter (KLA-Tencor P.16). Both sets annealed with *in situ* TAP at 450 ^{0}C for 5, 10, 15, and 20 min. $CdCl_2$ treatment carried out for these sets at 360 ^{0}C for 15 min. AFM, RS, Transmittance, band gap, *J-V* curve, QE and performance measurements were carried out to investigate the structural, optical, electrical, and overall performance properties of the solar cells.

3.1: CdS (120 nm)/CdTe (1.3 µm) Thin Film Set

3.1.1: AFM Measurement Results

The AFM micrographs of the as-deposited CdTe layer and four other devices synthesized at different iTAP conditions are compared in Figures 3-1. The as-deposited sample without any iTAP treatment has a smooth surface and a small grain size of ~50 nm, which is larger than the grain size of ~ 8.26 nm reported on CdTe films fabricated using imprinting and the electro-deposition method [39]. However, it is much smaller than the CdTe grain size of 3-4 µm in thick films deposited ~600 ^{0}C in the CSS process [29]. This may be attributed to the relatively high kinetic energy of atoms carried by the PLD plume, which is expected to enhance two-

dimensional growth. In addition, the lower substrate temperature used in the PLD is also beneficial to prevent 3D crystallization in an uncontrollable fashion. These are important to producing a continuous thin film at small thickness and preventing local island-type aggregation.

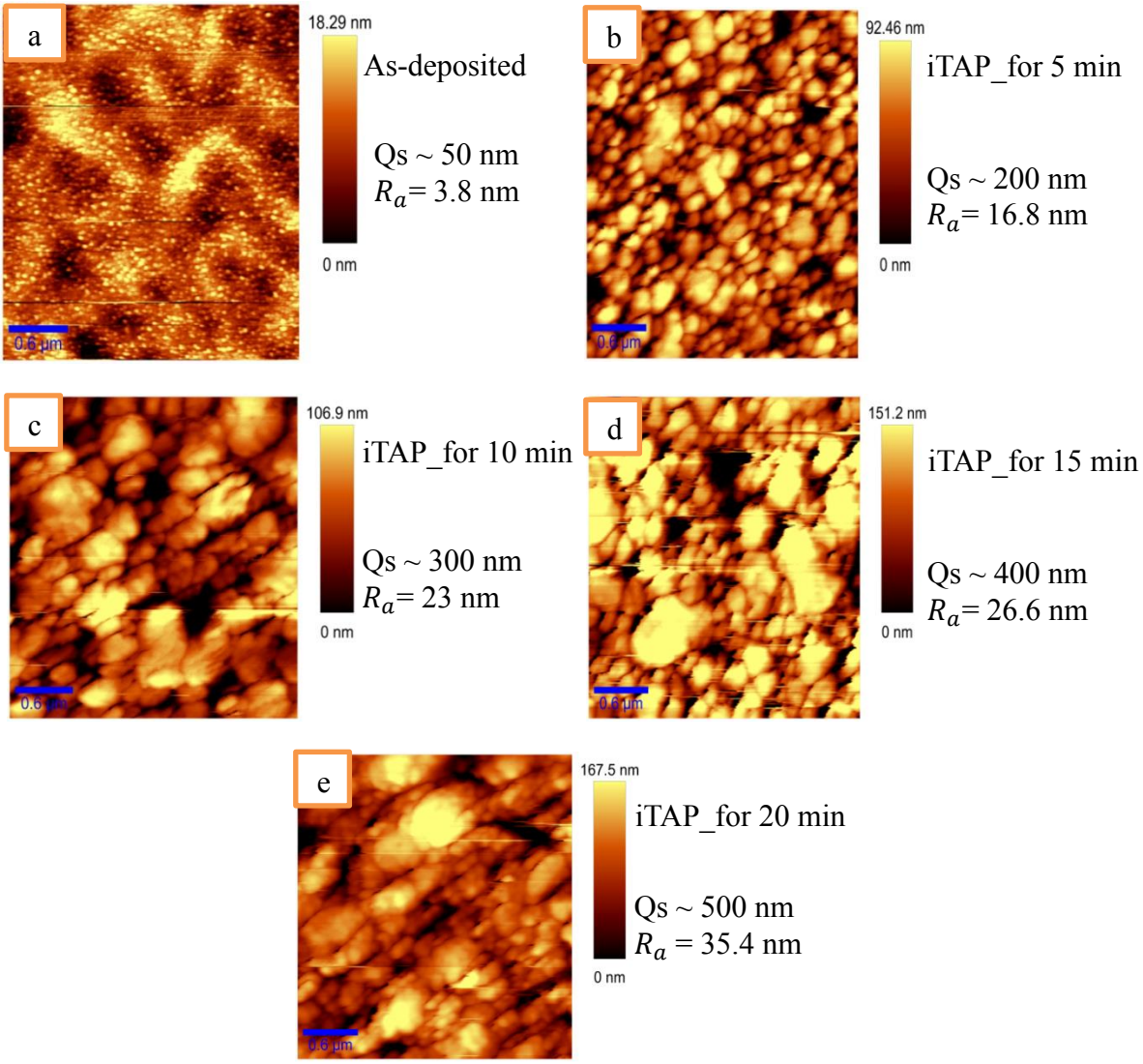

Figure 3-1: AFM images for CdTe films without (a) and with iTAP at 450 ^{0}C for different durations of 5 min. (b), 10 min. (c), 15 min. (d) and 20 min. (e), respectively.

The iTAP evidently promotes grain growth as shown in Figures 3-1b-3-1e and the grain growth increases monotonically with the iTAP duration at the fixed temperature of 450 ^{0}C. At 5 min. iTAP duration, the grain size increased to ~ 200 nm with appearance of many rounded facets. By increasing the iTAP duration to 10 min., even larger grain size of ~ 300 nm can be seen in Figure 3-1c, and a strong reaction seemed to be occurred when one could observe liquid-like coalescence and the formation of some voids. Further increasing the iTAP time up to 15 min. and 20 min. respectively as shown in Figures 3-1d and 3-1e, the formation of crystallized CdTe film with many large faceted crystallites can be clearly seen and grain size is ~ 500 nm with increased number of voids. Therefore, a consistent CdTe grain growth, film morphology change and improved CdS/CdTe heterojunction interface occurred with the increasing iTAP duration, leading to an increase of the shunt resistance (R_{sh}) and consequently an increase of the short current density (J_{sc}) and fill factor (*FF*) to be discussed later. It should be noted that the CdTe crystallization process is accompanied with an increase of the S and Te interdiffusion at the CdS/CdTe interface, which leads to reduction of the lattice mismatch and improvements of the depletion region and hence an increase of the open-circuit voltage (V_{oc}).

As a consequence of the microstructure evolution during the iTAP, the total sample thickness reduced by about 13% from 1.5 μm to 1.3 μm. Some additional effect re-evaporation surface at temperatures >275 ^{0}C [40].

In addition, the CdTe film surface roughness increased consistently with longer iTAP treatment. The As-deposited film has a surface roughness average of R_a= 3.8 nm. Larger R_a of 16.8 nm, 23 nm, 26.6 nm and 35.4 nm were observed after the iTAP at 450 ^{0}C for 5 min., 10 min., 15 min. and 20 min., respectively. Second, the possibility of forming pin-holes is increased

on the structure of the films after the iTAP. This fact can be concluded from the surface skewness (SSK) of AFM images, which describes the asymmetry of the height distribution histogram of films' structures. The as-deposited film has a small possibility of pin-holes and a positive value of SSK equal to 0.14, which indicates that this film has a flat surface with peaks. While after using iTAP, the values of SSK are -0.05, -0.37, -0.53, and -1.16 for films treated at 450 ^{0}C for 5 min., 10 min., 15 min., and 20 min. respectively. These negative values of SSK indicate that the structures of treated films show a bearing surface with holes. Therefore, it is clear from the AFM study that the iTAP is very important step to improve the morphology properties by produce large grain size, increase the surface roughness and reduce the mismatch, which enhance the solar cell parameters significantly. However, long duration of iTAP can enhance a material loss and voids formation.

After $CdCl_2$ treatment, further grain growth was produced as well as increasing in surface roughness. Figure 3-2 shows the AFM images of samples with and without $CdCl_2$ treatment at 360 ^{0}C for 15 min. and different iTAP conditions. These images show how the structure of films was affected by $CdCl_2$ treatment due to the temperature and $CdCl_2$ vapor diffusion onto films' structure. This process is very important to increase the doping of CdTe and block the channels and pinholes. Also, due to the high temperature, it has an important effect on the grain growth which resulted in a strong relation with the iTAP conditions. More explanations will be discussed later in this chapter about this relation.

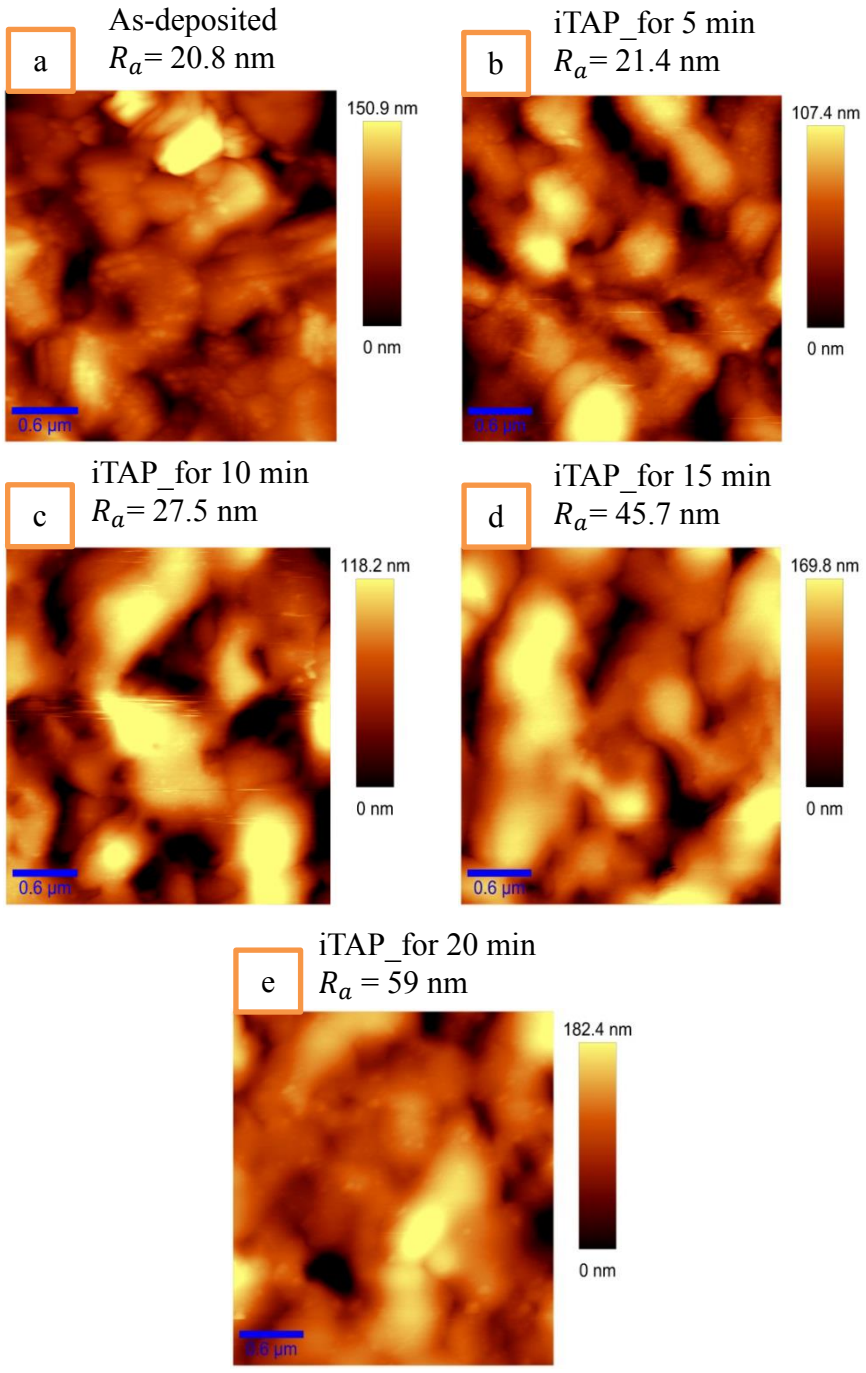

Figure 3-2: AFM images after $CdCl_2$ treatment at 360 ^{0}C for 15 min. for film without iTAP (a) and four other films iTAP treated at 450 ^{0}C with different duration: 5 min. (b), 10 min. (c), 15 min. (d) and 20 min. (e).

3.1.2: Raman Spectroscopy Results

The Raman spectra were taken by using WI-Tec AFM-Raman system with the wavelength of laser beam (λ_{exc} = 488 nm) on the CdTe samples to elucidate the details of the crystallinity and microstructure. Figure 3-3 compares Raman spectra of the as-deposited film and four other films treated with different iTAP duration. Four Raman signature peaks can be detected. The peaks at 141 cm^{-1} and 169 cm^{-1} correspond to the transverse optical (TO) and the longitudinal optical (LO) phonon of CdTe, respectively [41, 42]. The peak at 292 cm^{-1} is attributed to (2TO) phonon of CdTe, while the peak at 730 cm^{-1} can be assigned to (TeO_x) existence [43, 44].

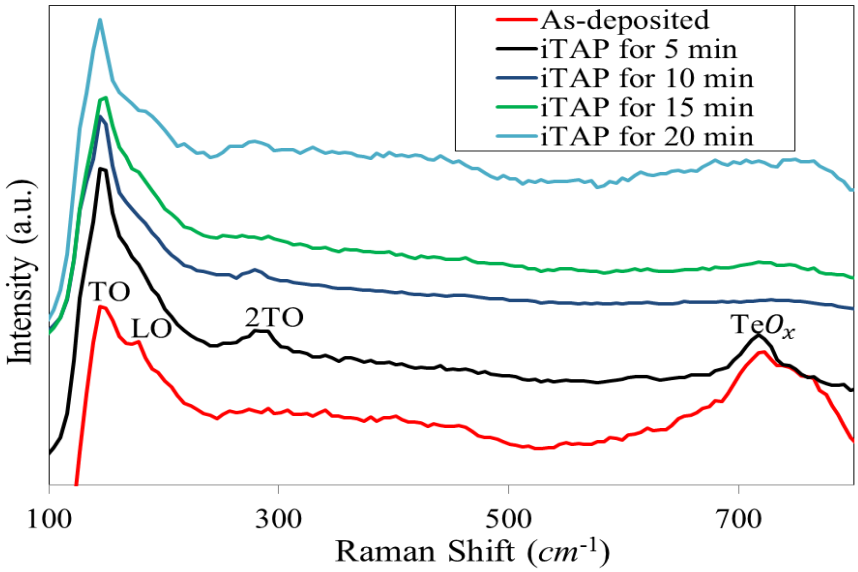

Figure 3-3: Raman spectra of five samples treated with different iTAP durations at 450 ºC. Peaks corresponding to the CdTe TO, LO, and 2TO modes as well as a signature peak of TeO_x can be observed at Raman shifts of 141, 169, 292 and 730 cm^{-1}, respectively.

The above Raman peaks can be studied according to the positions and selection rules of CdTe modes [45] as following: It is indicated that LO scattering is only allowed from (1 0 0) and

(1 1 1) planes, while TO scattering is only allowed from (1 1 0) and (1 1 1). Therefore, the as deposited film (red), which has both modes, can consist of both hexagonal and cubic planes. After the iTAP, the LO mode became negligibly detectable while the TO mode increased considerably after the iTAP. This, together with the appearing of the high order 2TO mode after the iTAP, indicates the microstructure improvement and recrystallization of the CdTe films with the iTAP treatment [44, 46]. Increasing the duration of iTAP up to 15 and 20 min. can enhance a random growth and poor crystal quality with decreasing the peaks' intensity at long duration. This behavior can affect the transportation paths of charge carrier, which can affect the (J_{sc}) and (*FF*). Moreover, it can be seen that the as-deposited films has a tellurium oxide (TeO_x) scattering, which may be attributed to oxidation of the CdTe during the PLD in presence of oxygen residues. This peak reduced with increasing iTAP duration and was completely eliminated after iTAP for more than 5 min.

3.1.3: Optical Measurement Results

The normalized transmission spectra (I/I_0) for CdTe films fabricated at different iTAP durations are shown in Figure 3-4. Distinctive differences are present between the as-deposited and iTAP treated samples. The former shows poorer transmittance in NIR region and poorer sharpness of the fall near the CdTe absorption edge. This may be observed for several reasons. First, the absorption mechanisms of the non-ideal interband transitions, which are attributed to the small grain growth and existence of many defects in the nano scaled crystal structure [47]. On the other hand, enhanced light scattering and light trapping may occur in films with smaller

grain dimensions [39]. The CdTe samples through different iTAP processing have comparable transmittance.

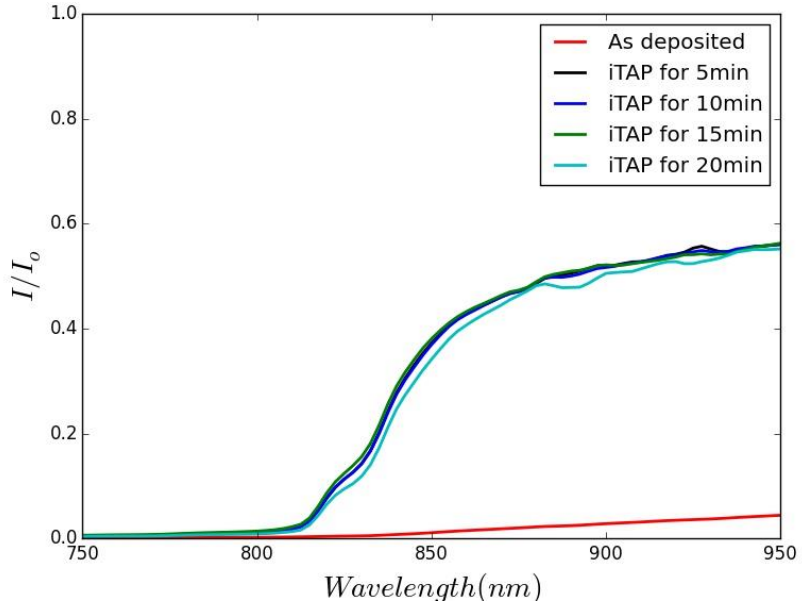

Figure 3-4: Transmittance spectra of CdTe thin films treated with iTAP at 450 ^{0}C for various durations.

The increment in the transmittance and sharpness of the *T*–λ curve near CdTe band edge for films that subjected to different iTAP conditions can be attributed to the absorption mechanisms of the ideal CdTe interband transitions, this was confirmed by the crystal improvements after iTAP in Raman study, and the considerable grain growth showed in the AFM results.

The band gap of CdTe can be estimated by using the Tauc equation [36]:

$$\alpha = (k/h\nu)\ (h\nu - E_g)^{n/2} \tag{3-1}$$

Where k is a constant, E_g is the band gap energy, n is a constant that equal to 1 for direct gap material such as CdTe and α is the optical absorption coefficient that can be calculated by using Beer-Lambert Law:

$$I = I_0 \exp(-\alpha t) \quad (3\text{-}2)$$

Where I , I_0 are the transmitted and incident radiation intensities, and t is the thickness. Thus, in Figure 3-5, CdTe band gap is approximated from the $(\alpha h\nu)^2$ against $h\nu$ plots by extrapolating the straight-line portion over the $h\nu$ axis.

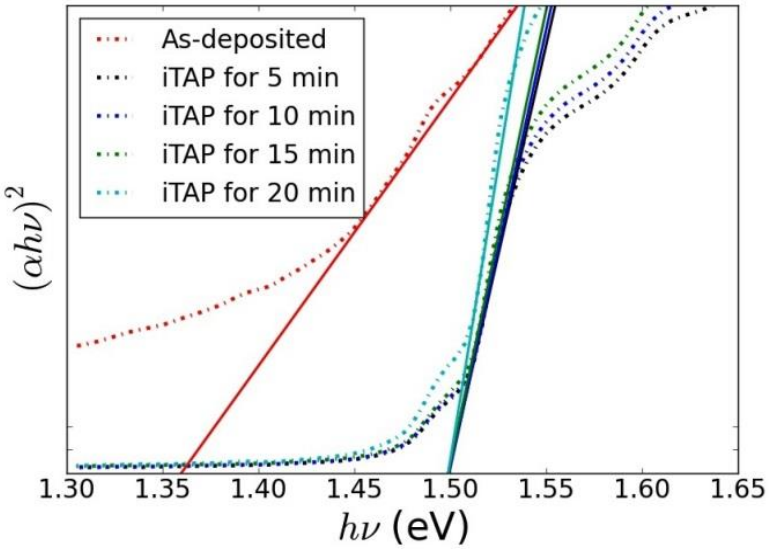

Figure 3-5: Band gap approximation of CdTe thin films treated with iTAP at 450 ^{0}C for various durations.

A considerably smaller E_g ~1.36 eV has been estimated for the as-deposited CdTe film, while all iTAP processed CdTe films have comparable E_g values close to that of the ideal CdTe bulk of ~1.5 eV (Table 3-1, next section). The smaller E_g of the former may be caused by the incomplete formation of CdTe structure fabricated at low temperatures. The application of the iTAP seemed effective in facilitating stoichiometric CdTe grain growth and improving its crystallinity.

While the CdTe crystallinity and optical absorption do not seem to vary significantly in the iTAP duration of 5-20 min., the CdTe microstructure evolution as consequence of the grain growth

with increasing iTAP duration has a profound effect on the solar cell performance including an increase of the shunt resistance (R_{sh}), and consequently an increase of the short current density (J_{sc}) and fill factor (*FF*). In particular, it should be noted that the CdTe crystallization and microstructure evolution process is accompanied with an increase of the S and Te inter-diffusion at the CdS/CdTe interface, which leads to reduction of the lattice mismatch and improvements of the depletion region and hence an increase of the open-circuit voltage (V_{oc}) [48].

3.1.4: *J-V* Measurement Results

Figure 3-6 compares the dark and illuminated (AM1.5) *J–V* characteristics of thin film CdTe solar cells with various iTAP durations. The specific performance of different cells is summarized in Table 3-1 and normalized illustration Figure 3-7. Higher V_{oc} was observed on all iTAP processed solar cells as compared to the reference device without iTAP. The increased V_{oc} may be attributed to the improved CdS/CdTe interface through inter-diffusion at the interface [49] facilitated by the iTAP, which is supported by the monotonic increase of the V_{oc} with increasing iTAP duration below 20 min. The best V_{oc} ~ 724 mV was obtained at 15 min. of iTAP duration. Interestingly, further increase in iTAP duration to 20 min. resulted in degraded V_{oc} ~ 605 mV, most probably due to the formation of voids and pinholes as suggested by the AFM data. This suggests the importance of iTAP in controlling the CdS/CdTe microstructure to achieve optimal CdTe grain size, connectivity, and its interface with CdS and to prevent formation of voids and pinholes as shunting paths in the CdS/CdTe solar cells.

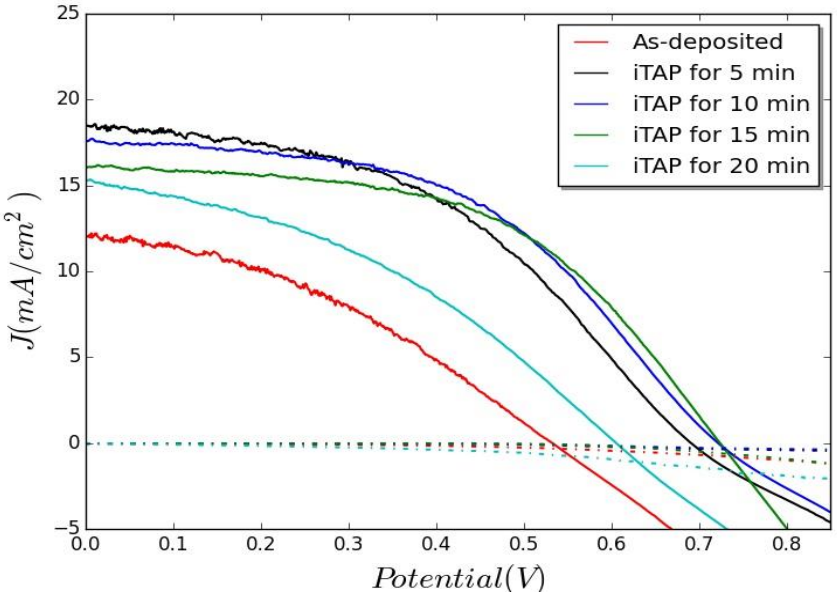

Figure 3-6: *J-V* curve characteristics of thin film CdS/CdTe solar cells with various iTAP durations of 0-20 min.

Table 3-1: Performances of thin film CdS (120 nm)/CdTe (1.3 μm) solar cells treated with iTAP at 450 ºC for various durations.

iTAP-Temperature (ºC)	**iTAP-Time (min)**	**CdTe - Band gap (eV)**	**V_{oc} (mV)**	**J_{sc} (mA/ cm^2)**	**FF (%)**	**Efficiency (%)**
0	0	1.40	546	12.9	37	2.59
450	5	1.50	691	18.5	45.5	5.8
450	10	1.50	722	17.6	49.6	6.3
450	15	1.50	724	16.1	52.7	6.13
450	20	1.50	605	15.3	38.1	3.52

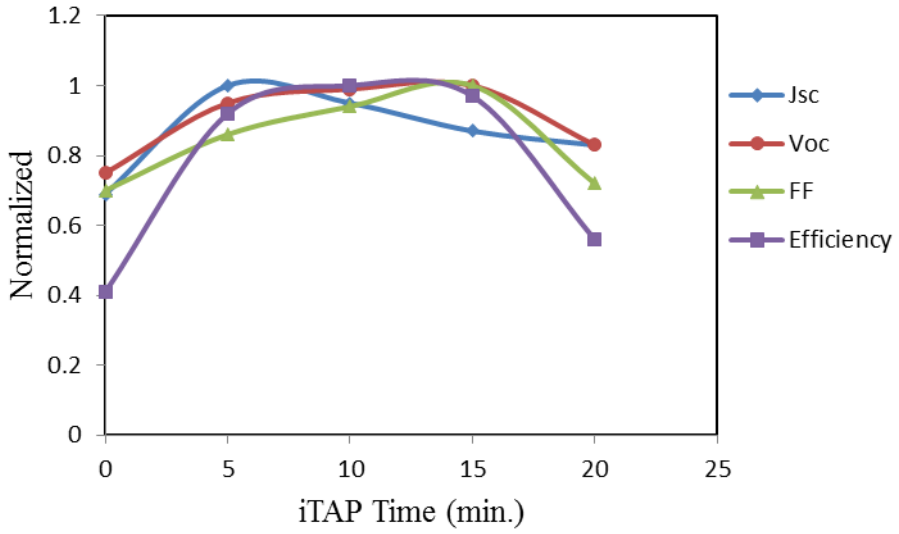

Figure 3-7: Behavior of solar cells preformance under iTAP at T= 450 ^{0}C for different durations.

Qualitatively, a similar trend in the J_{sc} and *FF* as functions of the iTAP duration were also observed despite some quantitative differences as shown in Figure 3-7. Basically, both J_{sc} and *FF* increased with iTAP duration in shorter time range, followed with a monotonic decrease in longer time range after passing a plateau. The best J_{sc} of 18.5 mA/cm^2 was observed at the iTAP duration of 5 min. while the best *FF* of 52.7 % was at the iTAP duration of 15 min. The increment in (J_{sc}) and (*FF*) of the devices that treated with iTAP at high temperature is attributed with the reduction of the grain boundaries due to the considerable grain growth shown in AFM images. Reducing these boundaries, that can work as recombination centers and trap states, is very important to reduce the charge carrier recombination and significantly enhance the shunt resistance R_{sh}, as shown in *J-V* curves. Also, it can be attributed to the decreasing of the serious resistance R_s due to producing better contacts.

Considering the similar optical absorption properties in these iTAP treated samples, the trend in J_{sc} vs. iTAP duration may be attributed to the recrystallization of CdTe planes which might become in un-preferable orientation at longer treatments, and to the correlation between iTAP and the follow-up ex situ $CdCl_2$ annealing, leading to the variation in J_{sc}. The reducing of the boundaries led to reduce the $CdCl_2$ vapor diffusion into CdTe structure during the $CdCl_2$ treatment. This is based on the fact that the diffusion of elements in polycrystalline materials is much faster through the grain boundaries because their incomplete axis than the bulk [50, 51]. These grain boundaries offer low resistance pathways for diffusing $CdCl_2$ and other elements in polycrystalline CdTe films. Thus, $CdCl_2$ diffusion into CdTe polycrystalline structure during $CdCl_2$ treatment is much likely to occur larger in small-grain CdTe films, than in larger-grained films and single crystal CdTe. As a result of reducing the $CdCl_2$ diffusion into CdTe structure, the doping of CdTe layer is reduced and less charge carries can be produced, which affects the J_{sc}. Therefore, it can be concluded that the iTAP at high temperature and $CdCl_2$ treatment is strongly depended on each other in terms of the grain growth and elements migration.

To check that, the last device in Table 3-1 was fabricated again but this time with longer $CdCl_2$ treatment, 20 min., to allow more $CdCl_2$ elements diffusion into the large-grain CdTe structure. The resulted *J-V* curve properties are shown in Figure 3-8, and the solar cell parameters are shown in Table 3-2.

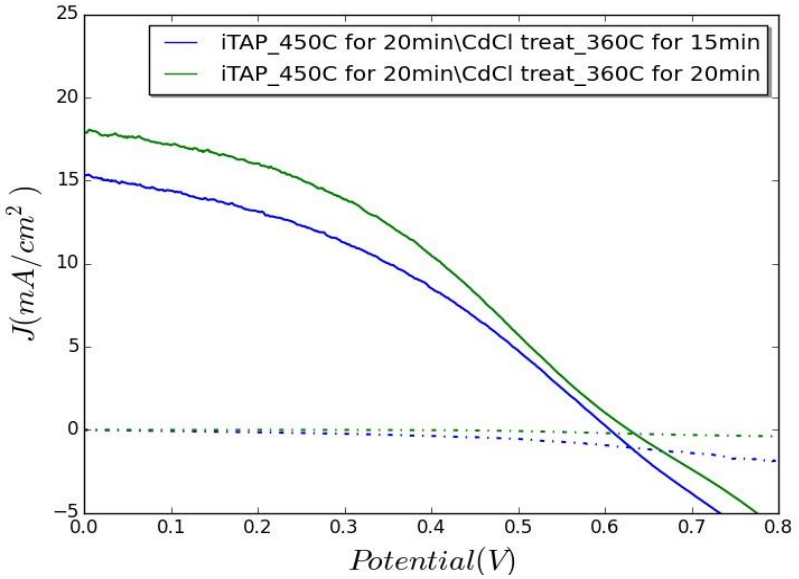

Figure 3-8: *J-V* curve characteristics of CdS/CdTe solar cells annealed with different $CdCl_2$ durations.

Table 3-2: Performances of thin-film CdS/CdTe solar cells treated with iTAP at 450 ^{0}C for 20 min. The $CdCl_2$ treatment is done at 360 ^{0}C for 15 min. and 20 min. The thickness of CdTe films is 1.3 μm.

$CdCl_2$ Treatment		**iTAP at 450 ^{0}C for 20 min**			
Temperature (^{0}C)	**Duration (min)**	**J_{sc} (mA/ cm^2)**	**V_{oc} (mV)**	**FF (%)**	**Efficiency (%)**
360	15	15.3	605	38.1	3.527
360	20	17.85	627	38.7	4.333

These results show that the (J_{sc}) of film that subjected to longer duration of iTAP and longer $CdCl_2$ treatment, 20 min., is improved. Thus, it can be concluded that both the post deposition iTAP and $CdCl_2$ treatments are connected to each other, and play an important role to

improve the performance of thin-film CdS/CdTe solar cells. An optimization of these two treatment process will be probably in our future research lists.

Finally, high efficiency up to 6.3% was obtained from thin-film CdS (120 nm)/ CdTe (1.3 μm) solar cells treated with iTAP at 450 ^{0}C for 10 min as it was shown in Table 3-1.

3.1.5: EQE Measurement Results

In Figure 3-9, the external quantum efficiencies (QE) of the same set of devices are depicted as function of wavelength. Considerable improvements in the spectral response of all iTAP treated samples at wavelengths of 520-800 nm can be clearly seen. This corresponds to an increase in charge carrier generation in the iTAP treated CdS/CdTe solar cells, which is anticipated from the crystallinity and microstructure improvements. In particular, the best QE spectrum observed on the sample with an iTAP at 450 ºC for 5 min. seems consistent with the best J_{sc} value observed on this sample.

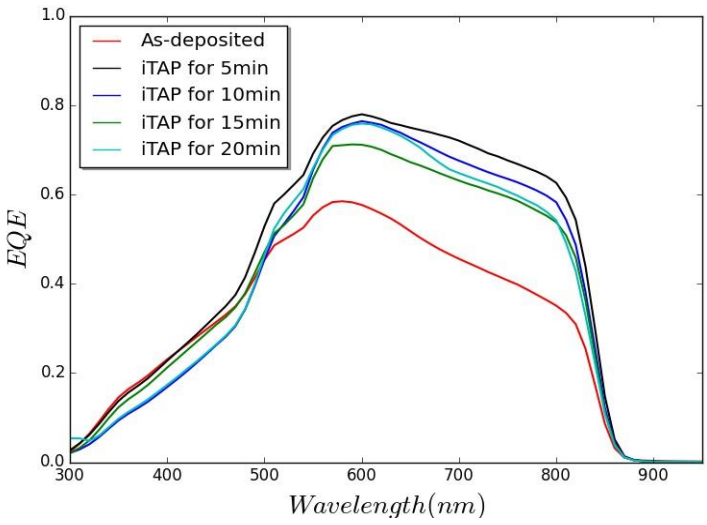

Figure 3-9: Quantum Efficiency curves of thin film CdS/CdTe solar cells treated with iTAP at 450 ^{0}C for various durations.

At longer iTAP duration, (10, 15, 20) min, spectral response in this range decreases gradually, which is supported by the decreasing in the J_{sc} values at these durations. Again this can be attributed to the change of the recrystallization of the planes' orientation in iTAP for long duration as showed in Raman study, and to the un-optimized $CdCl_2$ treatment at high temperatures.

3.2: CdS (120 nm)/CdTe (0.75 µm) Thin Film Set

In the next step, ultra-thin films based of CdS (120 nm)/CdTe (0.75 µm) solar cells samples were fabricated in the same way and treated with the same iTAP at 450 ^{0}C for 5 min., 10 min., 15 min., and 20 min. and $CdCl_2$ treatment at 360 ^{0}C for 15 min. This step was done to investigate and study the effect of reducing CdTe thickness on the absorption mechanism, the charge carrier recombination process, and how iTAP can play a role in microstructural properties of different CdTe thicknesses.

3.2.1: Results and Discussion

AFM, Raman spectroscopy and optical studies were carried out on all samples, and the properties of these studies were similar to the previous set. Therefore, electrical properties and *J-V* measurements will be presented in this section.

Figure 3-10 shows *J-V* curve properties of all the samples under different iTAP durations. It is obvious that there are considerable improvements in all iTAP-treated samples. These improvements are due to the crystallizations and grain growth which produce less grain boundaries and less charge carrier recombination.

In Table 3-3, the solar cell parameters are shown, which exhibit very significant improvements after the iTAP for the same pervious reasons and resulted in high solar cells performance.

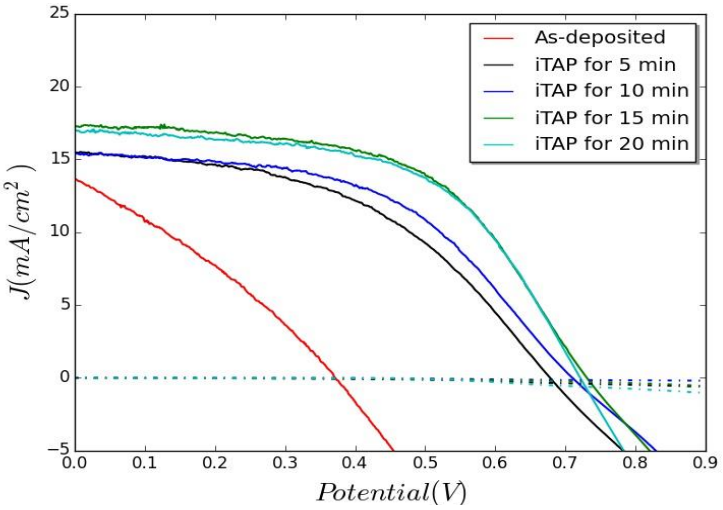

Figure 3-10: *J-V* curve characteristics of ultra-thin film CdS/CdTe solar cells treated with iTAP at 450 ^{0}C for various durations.

Table 3-3: Performances of ultra-thin film CdS/CdTe solar cells treated with iTAP at 450 ^{0}C for various durations. The $CdCl_2$ treatment is done at 360 ^{0}C for 15 min. The thickness of CdTe films is 0.75 μm.

iTAP-Temperature (^{0}C)	**iTAP-Time (min.)**	**J_{sc} (mA/cm^2)**	**V_{oc} (mV)**	**FF (%)**	**Efficiency (%)**
0	0	12.91	346	41.8	1.87
450	5	15.48	677	47.3	4.96
450	10	15.4	709	50.8	5.55
450	15	17.27	730	55.5	7
450	20	16.97	730	56.2	6.87

The following figure illustrates the trend and behavior of J_{sc}, V_{oc}, FF and general performance of solar cells samples treated with iTAP at 450 ^{0}C for different durations.

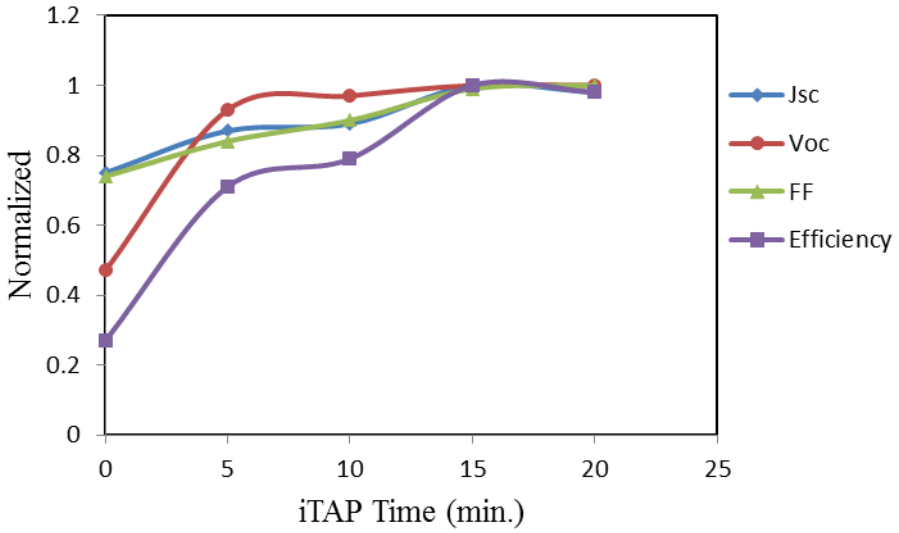

Figure 3-11: Behavior of solar cells performance under iTAP at T= 450 ^{0}C for different durations, CdTe thickness is 0.75 µm.

These results are very interested if we compare it with the results of the pervious set of CdS (120 nm)/CdTe (1.3 µm). As we reduced the CdTe thickness layer from 1.3 µm to 0.75 µm, the photon absorption should be reduced and this would affect the generation of the charge carrier leading to decrease the J_{sc}, V_{oc}, FF and the conversion efficiency. However, results shows that the solar cells in this case produce almost similar J_{sc} and V_{oc} and slightly better FF. And since FF is strongly depended on the recombination effect, we can conclude that reducing the absorption layer thickness has an advantage of reducing the recombination effect which affects the general performance of solar cells. An efficiency of 7% has been recorded from ultra-thin film based CdS (120 nm)/ CdTe (0.75 µm) treated with iTAP at 450 ^{0}C for 15 min.

Chapter 4 : Conclusions and Perspectives

In situ thermal annealing process (iTAP), a treatment process before the common *ex situ* cadmium chloride ($CdCl_2$) treatment, has been introduced to improve crystal quality and morphology of the CdTe thin films. A strong correlation between the two processes was observed, which has a profound effect on the performance of CdS/CdTe thin film solar cells. Atomic Force Microscopy and Raman Spectroscopy show that iTAP in the optimal window produces considerable CdTe grain growth and improves the CdTe crystallinity, which result in significantly improved optoelectronic properties and quantum efficiency of the CdS/CdTe solar cells. However, iTAP for longer duration can lead to material loss and voids formation, and hence degraded solar cell performance.

An efficiency of about 6.3% has been reported for thin film CdS (120 nm)/CdTe (1.3 µm) solar cells processed with iTAP at 450 ^{0}C for 10 min, and of about 7% has been recorded from ultra-thin film based CdS (120 nm)/ CdTe (0.75 µm) treated with iTAP at 450 ^{0}C for 15 min. Therefore, smaller CdTe thickness provides advantages in reduced charge recombination.

It should be noticed that using iTAP at higher temperatures, like 500 ^{0}C and 550 ^{0}C, has already been used in our lab and it didn't shows good results. This can be due to a strong crystal evolution that can be provided by these higher temperatures that can causes shunts and cells short, or due to a migration of big amount of material at p-n junction that causes layers consuming.

Moreover, since it is already proved that iTAP can significantly enhance the recrystallization in polycrystalline material such as CdTe thin film which led to improve the

overall performance of the solar cells, therefore, many possible perspectives can be motivated. For example, study the effect of iTAP on the CdS window layer structure by applying iTAP after its deposition in different thicknesses. This step can provide important information about the optimal conditions of iTAP that can control the crystallization, and also the amount of consumed CdS material due to high temperature used in TAP.

On the other hand, by applying iTAP on multi-thicknesses CdTe layer, interested results can be obtained about the optimal CdTe thickness that can be used for thin film solar cells. Further, using iTAP with different atmospheres, such as O_2, can be very important approach to investigate and study the effect of the chemical reaction together with the high temperature on the fabricated cells. These research perspectives and more will be in our next investigations to obtain solar cells based on CdTe thin-film with high performance.

REFERENCES

[1] R. Feynman, R. Leighton, and M. Sands. (1963). *The Feynman Lectures on Physics*. *Vol. 1 (Addison-Wesley, Menlo Park, California)*. Available: http://www.feynmanlectures.info/

[2] OECD/IEA, " 2013 Key World Energy Statistics (Paris, France, 2013)." *international energy agency*, 2013.

[3] OECD/IEA, "2014 Key World Energy Statistics " 2014.

[4] I. P. C. Change, *Climate Change 2013 - The Physical Science Basis: Working Group I Contribution to the Fifth Assessment Report of the Intergovernmental Panel on Climate Change*: Cambridge University Press, 2014.

[5] L. Freris and D. Infield, *Renewable energy in power systems*: John Wiley & Sons, 2008.

[6] A. Becquerel, "Recherches sur les effets de la radiation chimique de la lumiere solaire au moyen des courants electriques," *Comptes Rendus de LAcademie des Sciences,* vol. 9, pp. 145-149, 1839.

[7] A.-E. Becquerel, "Mémoire sur les effets électriques produits sous l'influence des rayons solaires," *Comptes Rendus,* vol. 9, p. 1839, 1839.

[8] C. E. Fritts, "On a new form of selenium cell, and some electrical discoveries made by its use," *American Journal of Science,* pp. 465-472, 1883.

[9] A. Einstein, "Über einen die Erzeugung und Verwandlung des Lichtes betreffenden heuristischen Gesichtspunkt," *Annalen der Physik,* vol. 322, pp. 132-148, 1905.

[10] R. S. Ohl, "Light-sensitive electric device," 1946.

[11] D. M. Chapin, C. S. Fuller, and G. L. Pearson, "A New Silicon p-n Junction Photocell for Converting Solar Radiation into Electrical Power," *Journal of Applied Physics,* vol. 25, pp. 676-677, 1954.

[12] D. Reynolds, G. Leies, L. Antes, and R. Marburger, "<title>Photovoltaic Effect in Cadmium Sulfide</title>," *Physical Review,* vol. 96, pp. 533-534, 10/15/ 1954.

[13] D. Jenny, J. Loferski, and P. Rappaport, "Photovoltaic Effect in GaAs p-n Junctions and Solar Energy Conversion*," *Physical Review,* vol. 101, pp. 1208-1209, 02/01/ 1956.

[14] J. A. Bragagnolo, A. M. Barnett, J. E. Phillips, R. B. Hall, A. Rothwarf, and J. D. Meakin, "The design and fabrication of thin-film CdS/Cu<inf>2</inf>S cells of 9.15-percent conversion efficiency," *Electron Devices, IEEE Transactions on*, vol. 27, pp. 645-651, 1980.

[15] A. Blakers and M. Green, "20% efficiency silicon solar cells," *Applied physics letters*, vol. 48, pp. 215-217, 1986.

[16] J. M. Olson, "Multilayer photoelectric cells," ed: Google Patents, 1987.

[17] K. Bertness, S. R. Kurtz, D. Friedman, A. Kibbler, C. Kramer, and J. Olson, "29.5%-efficient GaInP/GaAs tandem solar cells," *Applied physics letters*, vol. 65, pp. 989-991, 1994.

[18] R. R. King, C. M. Fetzer, P. C. Colter, K. M. Edmondson, J. H. Ermer, H. L. Cotal, *et al.*, "High-efficiency space and terrestrial multijunction solar cells through bandgap control in cell structures," in *Photovoltaic Specialists Conference, 2002. Conference Record of the Twenty-Ninth IEEE*, 2002, pp. 776-781.

[19] M. Wanlass, S. Ahrenkiel, D. Albin, J. Carapella, A. Duda, K. Emery, *et al.*, "GaInP/GaAs/GaInAs monolithic tandem cells for high-performance solar concentrators," in *Proc. International Conference on Solar Concentrators for the Generation of Electricity or Hydrogen*, 2005, pp. 1-5.

[20] M. Bosi and C. Pelosi, "The potential of III-V semiconductors as terrestrial photovoltaic devices," *Progress in Photovoltaics: Research and Applications*, vol. 15, pp. 51-68, 2007.

[21] S. O. Gaetan Masson (iCARES Consulting), Manoel Rekinger, "“Global Market Outlook for Photovoltaics
2014-2018,”" *European Photovoltaic Industry Association*, 2014.

[22] J. L. Gray, "The physics of the solar cell," *Handbook of photovoltaic science and engineering*, vol. 2, pp. 82-128, 2003.

[23] Nick84. (14 February 2013). *Solar spectrum*. Available: http://commons.wikimedia.org/wiki/File%3ASolar_spectrum_en.svg

[24] C. J. Chen, *Physics of solar energy*: John Wiley & Sons, 2011.

[25] B. E. McCandless and J. R. Sites, "Cadmium telluride solar cells," *Handbook of Photovoltaic Science and Engineering*, pp. 617-662, 2003.

[26] W. K. Metzger, D. Albin, M. J. Romero, P. Dippo, and M. Young, "CdCl2 treatment, S diffusion, and recombination in polycrystalline CdTe," *Journal of Applied Physics*, vol. 99, p. 103703, 2006.

[27] N. R. E. Laboratory. (2014). *NREL demonstrates 45.7% efficiency for concentrator solar cell*. Available: http://cdn.phys.org/newman/gfx/news/hires/2014/nreldemonstr.jpg

[28] M. A. Green, K. Emery, Y. Hishikawa, W. Warta, and E. D. Dunlop, "Solar cell efficiency tables (Version 45)," *Progress in Photovoltaics: Research and Applications*, vol. 23, pp. 1-9, 2015.

[29] C. S. Ferekides, D. Marinskiy, V. Viswanathan, B. Tetali, V. Palekis, P. Selvaraj, *et al.*, "High efficiency CSS CdTe solar cells," *Thin Solid Films*, vol. 361–362, pp. 520-526, 2/21/ 2000.

[30] P. R. Willmott and J. R. Huber, "Pulsed laser vaporization and deposition," *Reviews of Modern Physics*, vol. 72, pp. 315-328, 01/01/ 2000.

[31] yashvant. (3 October 2013). *Opensource Handbook of Nanoscience and Nanotechnology*. Available: The Opensource Handbook of Nanoscience and Nanotechnology

[32] D. Schroeder, "Semiconductor Material and Device Characterization 3rd edn(Hoboken, NJ," ed, 2006.

[33] *alpha300 RA – a unique combination of chemical and nanoscale imaging in one system.* Available: http://www.witec.de/products/raman/alpha300-ra-combined-raman-afm-imaging/

[34] P. Instruments, "Raman spectroscopy basics," *Internet: http://content. piacton. com/Uploads/Princeton/Documents/Library/UpdatedLibrary/Raman_Spectroscopy_Basics. pdf*, 2012.

[35] Moxfyre. (2009). *Molecular energy levels and Raman effect*. Available: http://en.wikipedia.org/wiki/Raman_spectroscopy

[36] H. T. Grahn, *Introduction to semiconductor physics*: World Scientific, 1999.

[37] C. Honsberg and S. Bowden, "Quantum Efficiency," *PV CDROM, pveducation. org*, 2010.

[38] Adnan Adla, "Instrumentation for quantum efficiency measurement of solar cells " *Newport Spectra-Physics GmbH, renewableenergy world.com,* 2010.

[39] S. Chun, K.-S. Han, J.-H. Shin, H. Lee, and D. Kim, "Fabrication and characterization of CdTe nano pattern on flexible substrates by nano imprinting and electrodeposition," *Microelectronic Engineering,* vol. 87, pp. 2097-2102, 11// 2010.

[40] S. K. Pandey, U. Tiwari, R. Raman, C. Prakash, V. Krishna, V. Dutta, *et al.*, "Growth of cubic and hexagonal CdTe thin films by pulsed laser deposition," *Thin Solid Films,* vol. 473, pp. 54-57, 2/1/ 2005.

[41] C. Ancora, P. Nozar, G. Mittica, F. Prescimone, A. Neri, S. Contaldi, *et al.*, "Properties of CdTe layers deposited by a novel method -Pulsed Plasma Deposition," 2011.

[42] M. Kimata, T. Suzuki, K. Shimomura, and M. Yano, "Interdiffusion of In, Te at the interface of molecular beam epitaxial grown CdTeInSb heterostructures," *Journal of Crystal Growth,* vol. 146, pp. 433-438, 1/1/ 1995.

[43] N. Dewan, V. Gupta, K. Sreenivas, and R. S. Katiyar, "Growth of amorphous TeOx($2 \leq x \leq 3$) thin film by radio frequency sputtering," *Journal of Applied Physics,* vol. 101, p. 084910, 2007.

[44] D. Wang, Z. Hou, and Z. Bai, "Study of interdiffusion reaction at the CdS/CdTe interface," *Journal of Materials Research,* vol. 26, pp. 697-705, 2011 Mar 14
2012-03-19 2011.

[45] B. Ghosh, S. Hussain, D. Ghosh, R. Bhar, and A. K. Pal, "Studies on CdTe films deposited by pulsed laser deposition technique," *Physica B: Condensed Matter,* vol. 407, pp. 4214-4220, 11/1/ 2012.

[46] T. M. Razykov, N. Amin, M. A. Alghoul, B. Ergashev, C. S. Ferekides, Y. Goswami, *et al.*, "Effect of the composition on physical properties of CdTe absorber layer fabricated by chemical molecular beam deposition for use in thin film solar cells," *Journal of Applied Physics,* vol. 112, p. 023517, 2012.

[47] M. Soliman, A. B. Kashyout, M. Shabana, and M. Elgamal, "Preparation and characterization of thin films of electrodeposited CdTe semiconductors," *Renewable Energy,* vol. 23, pp. 471-481, 7// 2001.

[48] B. E. McCandless, L. V. Moulton, and R. W. Birkmire, "Recrystallization and sulfur diffusion in CdCl2-treated CdTe/CdS thin films," *Progress in Photovoltaics: Research and Applications,* vol. 5, pp. 249-260, 1997.

[49] T. H. Myers, J. F. Schetzina, S. T. Edwards, and A. F. Schreiner, "Effect of surface preparation on the 77 K photoluminescence of CdTe," *Journal of Applied Physics,* vol. 54, pp. 4232-4234, 1983.

[50] P.G. Shewmon, "Diffusion in Solids (J. Williams Book Company, Janks, Oklahoma)," p. p. 164, 1983.

[51] H. Chou, A. Rohatgi, N. Jokerst, E. Thomas, and S. Kamra, "Copper migration in CdTe heterojunction solar cells," *Journal of electronic materials,* vol. 25, pp. 1093-1098, 1996.